Numerical and experimental study of a FORM-based design wave applying the HOS-NWT nonlinear wave solver

Shinwoong Kim, Benjamin Bouscasse, Guillaume Ducrozet, Maxime Canard, Guillaume de Hauteclocque, Charaf Ouled Housseine, Pierre Ferrant

Numerical and experimental study of a FORM-based design wave applying the HOS-NWT nonlinear wave solver

Shinwoong KIM[a], Benjamin BOUSCASSE[a,*], Guillaume DUCROZET[a], Maxime CANARD[a], Guillaume DE HAUTECLOCQUE[b], Charaf OULED HOUSSEINE[b], Pierre FERRANT[a]

[a]*Nantes Université, École Centrale Nantes, CNRS, LHEEA, UMR 6598, F-44000 Nantes, France*
[b]*Bureau Veritas, Paris, France*

Abstract

This paper presents a comparative study of long-time irregular waves and equivalent design waves (EDW) in terms of geometric similarity and probability of exceedance (POE) distribution of the wave crest. For a proper comparison between the two wave types, the same nonlinear model was applied in the wave generation by application of the Higher-Order Spectral-Numerical Wave Tank (HOS-NWT), a fully nonlinear propagation solver.

Numerical and experimental Monte-Carlo results were obtained through a number of realizations of a given sea state, and results were used as a reference for the EDW results. The experimental measurements and numerical simulations for a given sea state were analyzed and compared in terms of the wave spectrum estimation and the POE distribution of wave crests. The agreement between experimental and numerical results in wave quality seemed sufficient for it to be used as a reference for EDW cases.

The First-Order Reliability Method (FORM) approach was applied in the calculation of EDW. The geometrical similarity between the measured EDW wave signal and

*Corresponding author

the corresponding irregular wave signals measured in a given sea state was reviewed. It confirmed that the FORM-based EDW generates a comparable wave profile. In the statistical analysis, however, the results showed that for some EDW cases in relatively severe sea states, the POE estimates by the FORM method appeared to have conservative values compared to the Monte-Carlo reference POE distribution, whereas for the EDW cases in moderate sea states, the estimated POEs were in very good agreement with the empirical wave crest POE distribution of a given sea state.

1. Introduction

In designing marine and offshore structures, an irregular sea state in the time domain is reproduced from the wave spectrum data of a region of interest to observe the most probable extreme responses of the structure in that sea state. Following the assumption that a sea state of a given region follows a stationary process, the spectral density of the sea state can be defined with specific parameters which are variables of the shape function to be used in the geographic region of interest, in particular, the significant wave height H_s and the peak period T_p. The extreme events associated with a wave spectrum specified with these parameters depend on the duration of the measurement. A typical choice is a 3-hour storm.

The time-domain analysis of wave-induced structural responses computed from a 3-hour free surface elevation time series, however, is not long enough to be considered as a statistically reliable result for estimating the statistically converged certain event. The wave elevation time signal of a certain sea state varies depending on the phase of each wave frequency component, and the probability of exceedance (POE) curve of the wave crest obtained in each 3-hour time series will have various behaviors accordingly. In addition, the lower the probability of a wave crest event in a 3-hour wave signal, the greater the variance in POE value of the corresponding crest event

between each 3-hour simulation with a random phase set. This becomes even more evident in very harsh sea conditions with strong nonlinear effects. To put it in another way, with a randomly selected wave phase set, a variability of the sea-state and the corresponding structural responses can be observed. Thus, to obtain statistically reliable results for events where the probability is close to 10^{-3} (approximately 1000 waves are obtained in 3 hours for typical sea states), at least 30 realizations of 3-hour full-scale wave time series are required with different sets of wave phases (Korean Register (2017)). This method of analysis is referred to as a stochastic approach.

From a practical point of view, the main problem with the stochastic approach is that it is time-consuming and computationally costly. As an alternative to using long time series, a deterministic approach with equivalent design waves (EDW) has been introduced for the design of marine and offshore structures. The main concept is to induce the most probable extreme response corresponding to a specified exceedance probability level of a sea state by one short focusing irregular wave train. Several analytical and numerical models for EDW have been introduced, but the general idea behind each model and the parameters considered in the calculation process are quite similar. For instance, the NewWave method developed by Tromans et al. (1991) computes the most probable wave profile by application of the Slepian theory (see Lindgren (1984)). Hansen and Nielsen (1995) introduced the Most-Likely Wave (MLW) based on the NewWave theory but with conditioning on the random instantaneous frequency. When the instantaneous frequency is $\omega = m_1/m_0$ the mean wave frequency, the MLW corresponds to the NewWave profile. Several response conditional wave methods which take into account the response characteristics of interest, for example, the variance of the response spectrum or transfer function in the calculation of EDW were later introduced e.g. Critical Wave Episodes (Torhaug (1996)), Most Likely Extreme Response (MLER) (Adegeest et al. (1998)), and Most Likely

Response Wave (MLRW) (Dietz (2005)). The basic concept behind those methods is the application of a linear transfer function in the EDW calculation, thus the calculated EDW profile and EDW-induced response can be a good indicator for the estimation of nonlinear response. Further descriptions of each model can be found in Dietz (2005).

NewWave has been experimentally studied, and has been widely used in various applications (Walker and Taylor (2005); Zang et al. (2010); Hunt-Raby et al. (2011)). A method called Constrained NewWave literally constrains NewWave into regular or irregular waves. The main concept of Constrained NewWave is embedding the NewWave profile in a random sea to have an effect of previous waves. A limitation of the concept is that as nonlinear wave-wave interaction is expected, it is not easy to generate a targeted abnormal wave. Bennett et al. (2012) carried out a numerical and experimental study on the generation of abnormal waves with NewWave and Constrained NewWave. For each model, numerical calculations were first performed, and the comparative analysis was done with the experimentally measured wave profile of each method. The study showed that the measured NewWave was in agreement with the solution obtained with linear or second-order wave theory, whereas it was difficult to reproduce a targeted wave profile with the Constrained NewWave approach. The study also analyzed another method called 'optimized sea', a method to create a target abnormal wave by optimising the random phase of wave components of a random sea, and pointed out the limitations of NewWave and Constrained NewWave.

A calibration process to deterministically reproduce a given wave sequence was introduced by Schmittner et al. (2009). The iterative correction process was applied for not only the wave amplitude but also its phase following the phase corrective concept for the generation of a desired focusing wave at a target location proposed by Chaplin (1996). A method to trace the wavemaker's input motion back based

on the estimated wave spectrum data at the target location was considered. Long- and short-crested deterministic wave profiles were generated and compared with the actual wave scenario (Schmittner and Hennig (2012)). Overall, the experimental results were in good agreement, while the authors emphasized the need for a further process in wave calibration for the improved wave quality of a local extreme event. Clauss and Schmittner (2005) applied an overall similar process but sophisticated calibrations for local wave sequences that include the extreme wave scenarios of interest. Wave propagation very similar to the target wave profile was generated by setting criteria for the wave height, zero down crossing period, crest, and target time, although many iteration processes were required.

In the NewWave, a linear description of the free surface wave elevation is basically applied in the calculation, and second or higher-order effects have to be taken into account separately for large abnormal waves. Walker et al. (2004) conducted a study on the effect of the wave's higher-order contribution to the shape of a freak wave using the NewWave method. The NewWave was used as a first-order contribution, and correction for the higher-order contribution of the freak wave called New Year wave was estimated with Stokes-type corrections and exact second-order wave theory. The modified NewWave wave profile with the higher-order corrections up to fifth-order showed very good agreement with the measured New Year wave profile, whereas linear NewWave showed considerable discrepancy with the measurement. With linear or weakly nonlinear fluid models, the difficulty of reproducing a wave elevation time trace with sufficient accuracy in experiments or other nonlinear frameworks such as computational fluid dynamics (CFD) is a drawback. A solution is to use fully nonlinear methods, but this is only possible if the method used to compute the wave train is compatible with a generic nonlinear solver.

The first-order reliability method (FORM) was introduced as a possible solution

to the non-linearity related issue by Der Kiureghian (2000). As the FORM method allows the use of a nonlinear solution in the time domain, any hydrodynamic model in principle can be applied regardless of the degree of non-linearity. Ghadirian et al. (2017) carried out an experimental study focused on the second-order effect on the FORM-based EDW wave profile, and compared it with the shape of the NewWave as well as with irregular waves measured in a given sea state. As expected, the FORM-based EDW wave signal generating second-order wave elevation in the calculation proved to be more comparable with measured irregular waves, whereas only FORM-based EDW calculated with the linear wave elevation formula had difficulty generating a wave shape similar to that of the measurement. In addition, the study stressed the need to consider a higher (more than second) order term in the wave elevation when calculating the EDW with a large target crest (low probability of exceedance) in order to obtain a more accurate wave profile relative to measurement.

Jensen (2009) also conducted a study on the FORM method, but using stochastic procedures. Several procedures were compared to assess the vertical bending moment of a container ship with various analytical methods including FORM. It was found that FORM tended to estimate the conservative mean up-crossing rate. Agreement between the overall results and a Monte Carlo (ensemble of realizations) simulation of the flexible hull in waves was acceptable, showing that the FORM method provides a comparable solution for strongly nonlinear problems.

Considering the above-mentioned studies, this study focused mainly on the numerical and experimental validation of the practicality of a FORM-based EDW approach by comparing it with the stochastic approach conducted with a combination of wave spectrum and various random seed sets. Five sea states were considered, each of which consisted of 3 individual EDW cases corresponding to different POE levels. As part of the cross-validation of the EDW approach, basically the same EDW

cases were generated in the experiment as in the numerical wave tank. The results were then compared with each other and with reference long-time irregular wave results as well. The study focused particularly on a geometrical similarity review of the calculated EDW wave profile by directly comparing it with the corresponding irregular waves having a similar amplitude occurring in a given sea state. A second focus of this study was to compare the experimental and numerical results both in terms of exceedance probability (POE) distribution of wave crests obtained in given sea states and relevant EDW cases. The POE distribution of irregular wave crests for 5 sea states was analyzed both numerically and experimentally. The results were used as a reference POE curve for the POE of EDW cases which was estimated by an analytical expression introduced in the FORM method.

2. Equivalent Design Wave (EDW) approach

2.1. Linear design wave

The NewWave theory, introduced by Tromans et al. (1991), models an abnormal wave profile having the most likely extreme wave shape. Following the result obtained by Lindgren (1970) that the dominance of the most probable surface elevation is closely related to the increase in crest, the NewWave elevation at a target position x_0 and at a target time t_0 is formulated with the autocorrelation function $r(x-x_0, t-t_0)$ scaled by a target amplitude C_{target}:

$$\begin{aligned} \eta_{New}(x-x_0, t-t_0) =& C_{target}\, r(x-x_0, t-t_0) \\ =& C_{target}\, \frac{\sum_{i=1}^{N} S(f_i)\cos(2\pi f_i(t-t_0) - k_i(x-x_0))df}{\sigma^2} \end{aligned} \tag{1}$$

where $S(f_i)$, f_i, and k_i are the power spectral density, the wave frequency and the wavenumber of the i^{th} wave component and df is the frequency increment. σ^2 is the variance of the free surface elevation of a given sea state, and defined as follows:

$$\sigma^2 = \sum_{i=1}^{N} S(f_i)df \tag{2}$$

With the equations above, C_{target} is generated at the target position x_0 and at the target time t_0. The corresponding wave amplitude A_i for each wave component can be calculated as described below :

$$A_i = \frac{C_{target} S(f_i)df}{\sigma^2} \quad (i = 1, ..., N) \tag{3}$$

It is simply calculated based on the linear superposition of N wave components of a given wave spectrum. However, the linear superposition method involves the issue of accuracy of the solution, thus it is necessary to consider a second or higher-order term for large abnormal wave cases in which the higher-order effect of the wave becomes significant (Walker et al. (2004)). For severe wave conditions, the nonlinear wave effects become important, Jensen and Capul (2006) also suggested applying additional corrections to account for this non-linearity of the waves in the FORM method. However, in this study, a different approach is taken. The non-linearity is considered through the use of a nonlinear wave propagation solver applied with the FORM minimization procedure.

2.2. Design wave with FORM

The FORM approach is considered an effective solution when the response (structural/hydrodynamic) distribution is not explicitly known, which is true when the problem is nonlinear. In that case, an EDW analytical expression cannot be derived and a minimization process needs to be performed. Thanks to the FORM approach, any response, in theory, can be estimated in the time domain regardless of its non-linearity (Jensen and Capul (2006)). Based on a given sea state and a properly defined hydrodynamic model of interest, the FORM calculates a deterministic short

irregular wave train yielding the specified event. In addition, the probability of exceedance of the specified target crest generated by EDW can be estimated from the procedure.

2.2.1. Input process

A typical way to generate nonlinear waves is through the use of a numerical wave tank (NWT). Assuming 2D wave propagation, it is composed of a wavemaker on one side and an absorbing beach on the opposite side. The wave generation is controlled by the wavemaker motion $X(t)$, defined in Eq. (4). This will be the Gaussian input of the FORM procedure.

$$\begin{aligned} X(t) &= \sum_{i=1}^{N} \frac{A_i}{\mathrm{TF}_i} \cos(2\pi f_i t + \xi_i) \\ &= \sum_{i=1}^{N} (u_i c_i(t) + \bar{u}_i \bar{c}_i(t)) \end{aligned} \tag{4}$$

where TF_i is the wavemaker transfer function, $u_i, \bar{u}_i$ are the uncorrelated and normal distributed parameters, which are related to the wave amplitude and phase A_i and ξ_i:

$$\begin{aligned} \frac{A_i}{\mathrm{TF}_i} &= \sigma_i^{wm} \sqrt{u_i^2 + \bar{u}_i^2} \\ \xi_i &= \tan^{-1}(\bar{u}_i / u_i) \end{aligned} \tag{5}$$

$c_i(t)$ and $\bar{c}_i(t)$ for each frequency component can be expressed as follows:

$$\begin{aligned} c_i(t) &= \sigma_i^{wm} \cos(2\pi f_i t) \\ \bar{c}_i(t) &= -\sigma_i^{wm} \sin(2\pi f_i t) \\ (\sigma_i^{wm})^2 &= \frac{S(f_i)}{{\mathrm{TF}_i}^2} df \end{aligned} \tag{6}$$

where σ_i^{wm} denotes the variance of each frequency component of the wavemaker motion. $S(f)$ and df are the wave spectrum and the constant increment between wave frequencies.

2.2.2. Limit state function

Once the wavemaker input process has been defined, FORM will look for a standard normal vector set, $\mathbf{u} = \{u_i, \bar{u}_i\} = \{u_1, \bar{u}_1, u_2, \bar{u}_2, ..., u_N, \bar{u}_N\}$ generating a given target crest C_{target} at a target position x_0 and at a target time t_0 with the highest probability among a number of $\{u_i, \bar{u}_i\}$ sets. The limit state function can be used to estimate a solution as expressed below (Der Kiureghian (2000)):

$$G(\mathbf{u}) \; = \; C_{target} - \eta_{HOS}(x_0, t_0|\mathbf{u}) = 0 \tag{7}$$

$\eta_{HOS}(x_0, t_0|\mathbf{u})$ is calculated by the nonlinear wave solver HOS-NWT (see Section 3.1). It is the wave elevation computed with a peak crest at $t = t_0$ and $x = x_0$.

In Figure 1, the limit state surface in u-space is defined with a number of $\{u_i, \bar{u}_i\}$ sets. The design point is where the distance from the point on the surface border G($\mathbf{u}$)=0 to the origin is the shortest among the realizations. This point is sought with FORM linearisation. Therefore, the FORM approach consists in finding the design point $\mathbf{u}^*$ which is a solution for the following optimization problem:

$$\beta = \min \sqrt{\sum_{i=1}^{N} (u_i^2 + \bar{u}_i^2)} \qquad \text{subject to} \qquad G(\mathbf{u}) = 0 \tag{8}$$

The deterministic EDW wave episode yielding a specified target crest C_{target} is obtained thanks to the design point $\mathbf{u}^*$ solution of the optimization problem. This shortest distance is called the FORM reliability index (or most probable point),

β_{FORM}, a function of $\{u_i^*, \bar{u}_i^*\}$ expressed in Eq. (9).

$$\beta_{FORM} = \sqrt{\sum_{i=1}^{N}(u_i^{*2} + \bar{u}_i^{*2})} \qquad \text{and} \qquad G(\mathbf{u}^*) = 0 \tag{9}$$

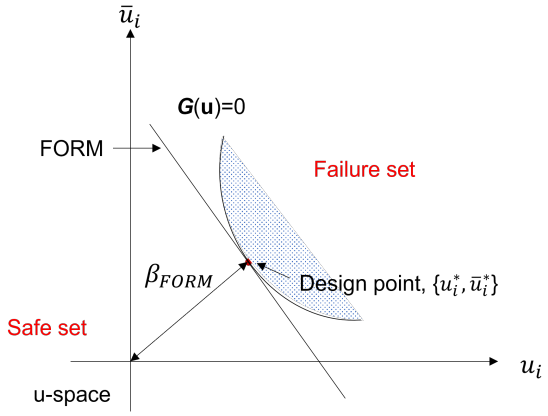

Figure 1: Limit state function **G** and β_{FORM} in u-space, Der Kiureghian (2000)

2.2.3. Mean up-crossing rates and exceedance probability

The mean out-crossing rate of the target crest, $\nu(C_{target})$ in a sea state of interest can be estimated with β_{FORM} and a set of $\{u_i^*, \bar{u}_i^*\}$:

$$\nu(C_{target}) = \frac{1}{2\pi\beta_{FORM}} e^{-\frac{1}{2}\beta_{FORM}^2} \sqrt{\sum_{i=1}^{N}(u_i^{*2} + \bar{u}_i^{*2})(2\pi f_i)^2} \tag{10}$$

Concerning the exceedance probability of the target crest in a given sea state having a narrow banded wave spectrum, the number of zero-up crossing events corresponds to the number of peaks M in a given time T, with $M = \nu(0)T$. In the same context, the number of out-crossing events exceeding the target crest corresponds to $m = \nu(C_{target})T$. Thus, the exceedance probability of the individual response C_{target} in a given time T can be expressed as a ratio of $\nu(C_{target})$ to $\nu(0)$ as expressed in Eq. (11).

By selecting several C_{target} in a given sea state, the distribution of POE estimated by FORM can be obtained, and a comparison with the empirical POE distribution of the corresponding sea state can be performed.

$$\begin{aligned} \text{Prob}(\text{C}< C_{target}) &= \text{CDF}(C_{target}) = 1 - \nu(C_{target})/\nu(0) \\ \text{Prob}(\text{C}> C_{target}) &= \text{POE}(C_{target}) = 1 - \text{CDF} \end{aligned} \tag{11}$$

where $1/\nu(0)$ is a zero-crossing period T_z calculated using target spectrum data.

3. FORM-based EDW with HOS-NWT

The main focus of the present study was to implement a FORM-based EDW wave approach using a fully nonlinear wave solver. The solver chosen here is the efficient and accurate open-source solver, Higher-Order Spectral - Numerical Wave Tank (HOS-NWT). To this aim, the input process and the resolution algorithm to find the design point are detailed. The advantage of using the nonlinear wave solver is that the numerically computed wave elevation can in principle be reproduced deterministically in the experimental wave tank.

3.1. HOS-NWT

The Higher-Order Spectral (HOS) method (Dommermuth and Yue (1987) and West et al. (1987)) was introduced to solve nonlinear wave propagation in time in an open fluid domain. Potential fluid theory is the basis of the method, thus the fluid is assumed to be incompressible and inviscid satisfying the Laplace equation $\Delta\phi = 0$. Although the original HOS method can solve highly nonlinear wave evolutions, its application was limited to the unbounded fluid domain defined with periodic boundary conditions with the prescribed initial free surface elevation $\eta(x, t = 0)$. Thus, to extend the application range of HOS and in order to enable comparison with experiment, HOS in a numerical wave tank (HOS-NWT) was developed (Ducrozet

et al. (2006)). A number of studies have been carried out on various configurations and have validated that the open-source HOS-NWT provides an accurate solution with efficient computational effort thanks to the FFT based scheme (Bonnefoy et al. (2010); Ducrozet et al. (2016); Suret et al. (2020)).

In the case of actual wave conditions, when the steep wave continues to develop or when its speed reaches a certain limit, a breaking wave can occur, which is associated with (strong) wave energy dissipation and the generation of vorticity. The problem, however, is that with simplified numerical models it is impossible to simulate the complex underlying physics of the breaking events. HOS-NWT is such a case, as it is defined based on the potential fluid theory modelling the wave propagation and evolution without taking into account the viscosity of the fluid particles. As a solution to these limitations, an eddy viscosity model was applied to HOS-NWT, following Tian et al. (2010), Seiffert et al. (2017), and Seiffert and Ducrozet (2018).

3.1.1. Wave calibration

Computing a fully nonlinear solution of the wave elevation in time and space is one subject of this study. Given that the wave field is a stationary process at each location of the wave tank, the calibration of the wave spectrum at a certain reference position can be performed from a pure stochastic point of view. This may however involve the need for some corrections to the wavemaker inputs to realize the target spectrum at the target location.

The target position located at x_0 from the wavemaker, where an environmental condition should meet the target condition depends also on practical reasons (such as the experimental setup and the length of the tank). A calibration methodology will modify the spectrum at the wavemaker (calibrated $S_{wm}(f)$) to achieve the target spectrum $S_{targ}(f)$ at the target position x_0. The iterative process is performed

straightforwardly by applying the correction factor corresponding to the ratio of the target amplitude to the measured amplitude. Further details can be found in Canard et al. (2022).

3.2. HOS-NWT with FORM

As a first step of the numerical algorithm (see Figure 2), a target crest C_{target} having a specific exceedance probability level in a sea state of interest is selected based on the Forristall distribution. Then, by applying the NewWave method (Eq. (3)) with C_{target} and the wave spectrum of interest, the set of amplitudes and the corresponding phases of each wave frequency component ($=\mathbf{u}^0$) are first calculated to define the initial wavemaker motion. Once the initial wavemaker motion has been defined, the algorithm starts to iterate with successive HOS-NWT simulations to find the most probable point (MPP), $\mathbf{u}^*$ with a criterion in β as follows:

$$\beta^{k+1} - \beta^k < 0.002 \tag{12}$$

where k corresponds to the k^{th} iteration. Initial β is set to 0, and in the subsequent iteration, it is replaced by the newly calculated value with a set of $\{u_i, \bar{u}_i\}^k$ using Eq. (8).

$$G(\mathbf{u}^k) = C_{target} - \eta_{HOS}(x_0, t_0|\mathbf{u}^k) \tag{13}$$

At every iteration step of the EDW calculation process, $\mathbf{u}^*$ is sought by running HOS-NWT. In detail, with $\mathbf{u}^k$ in the k^{th} iteration, the wave time series $\eta_{HOS}(x_0, t\text{-}|\mathbf{u}^k)$ at the target position x_0 is exported to compare its elevation at the target time t_0, $\eta_{HOS}(x_0, t_0|\mathbf{u}^k)$ with C_{target} (Eq. (13)). If the $\mathbf{u}^k$ meets the tolerance criterion in β (Eq. 12), the iteration process ends and provides outputs, namely i) the wave elevation time series $\eta_{HOS}(x_0, t|\mathbf{u}^*)$ inducing C_{target} at the target time t_0 and ii)

the corresponding wave spectrum at the wavemaker. Thus, the wave time series calculated at the target position represents the reference by itself. In other words, EDW data from the process applied above do not require additional wave calibration.

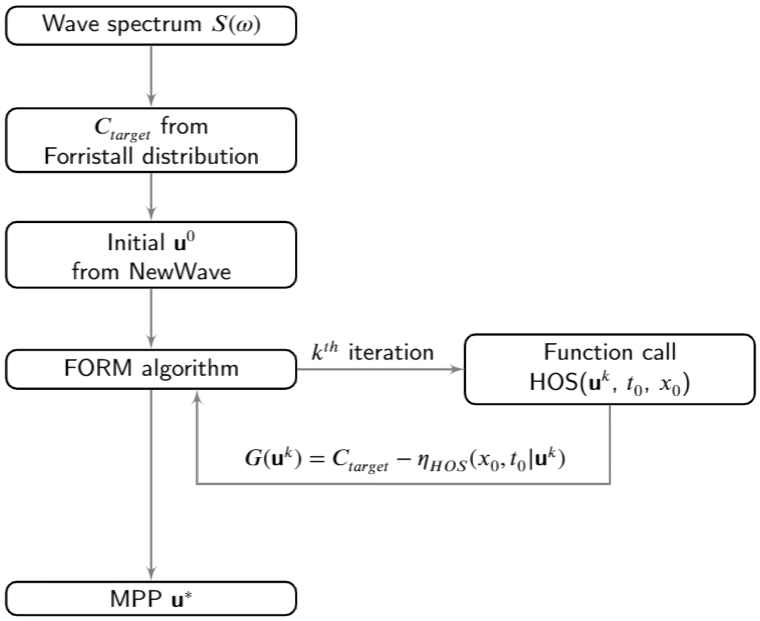

Figure 2: HOS coupling with FORM

3.3. FORM algorithm for most probable point (MPP) search

3.3.1. Background of the algorithm applied

The numerical algorithm applied in this study is based on a specific class of FORM optimization algorithms named HL as shorthand to denote the algorithm proposed by Hasofer and Lind (Hasofer and Lind (1974)). Although the HL-based algorithms have been shown to be efficient, it sometimes shows instability depending on the application case. (Lemaire (2013)). Therefore, it was necessary to introduce some slight modifications in the algorithm to improve its robustness with a reasonable CPU cost. In this respect, Liu and Der Kiureghian (1991) proposed the application

of the merit function in their MHLRF algorithm. However, in this algorithm, $\nabla G(\mathbf{u})$ is required at each internal loop iteration, This results in a huge number of function calls, which is proportional to the number of optimization components. For this reason, the MHLRF algorithm is considered to be expensive since many function calls are needed to evaluate $\nabla G(\mathbf{u})$ (Jensen et al. (2017)).

To overcome this additional CPU cost, Jensen et al. (2017) suggested using the HLCL algorithm which computes $\nabla G(\mathbf{u})$ only once per iteration. As a result, a considerable reduction in CPU time is achieved (Jensen et al. (2017)) by avoiding gradient computation. Despite this important advantage, while coupling HLCL with HOS-NWT, it was noted that the algorithm applying the secant method failed during the line search stage after a few iterations, in particular for the cases with a high HOS order $M > 2$, even with a reasonable H_s value. This problem is related to the use of the zero search algorithm which does not converge when the limit state function G has a high convexity variation (e.g Figure 3). In this case, the secant algorithm keeps oscillating between two solutions or leads to unrealistic wave elevation values causing HOS simulation divergence. This behavior was observed during the tests.

3.3.2. Modified Hasofer and Lind with Goldstein-Armijo (MHLGA) algorithm

As outlined above, an HL-based algorithm denoted MHLGA was implemented in the present study. The MHLGA procedure benefits from the previous two algorithms that i) uses a merit function to avoid the zero search procedure and ii) does not require any gradient evaluation of G. With this in mind, we can introduce the following merit function (Santos et al. (2012)):

$$m(\mathbf{u}) = \frac{1}{2}\left\|\mathbf{u}\right\|^2 + \frac{c}{2}G(\mathbf{u})^2 \tag{14}$$

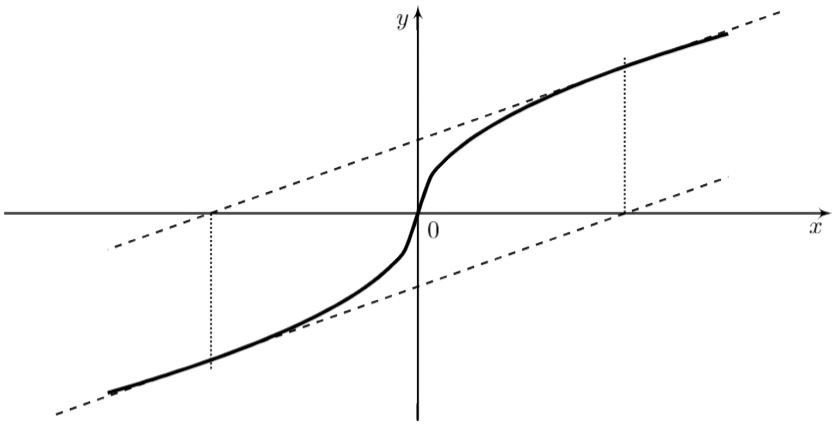

Figure 3: Example of Newton's / secant method failure, the algorithm remains stuck in an infinite loop

The optimal design point $\mathbf{u}^*$ is determined using a line search procedure (Liu and Der Kiureghian (1991)):

$$\mathbf{u}^{k+1} = \mathbf{u}^k + \alpha^k \mathbf{d}^k \tag{15}$$

with

$$\mathbf{d}^k = \frac{1}{\|\nabla G(\mathbf{u}^k)\|^2} \left(\nabla G(\mathbf{u}^k).\mathbf{u}^k - G(\mathbf{u}^k)\right) \nabla G(\mathbf{u}^k) - \mathbf{u}^k \tag{16}$$

where the superscript k denotes the k^{th} iteration. α^k is determined through a line search in the $\mathbf{d}^k$ direction to decrease $m(\mathbf{u}^k)$ as:

$$m(\mathbf{u}^k + \alpha^k \mathbf{d}^k) < m(\mathbf{u}^k) \tag{17}$$

It has been proved that $\mathbf{d}^k$ is a descent direction for this merit function at any $\mathbf{u}$ point under the following condition (Santos et al. (2012)):

$$c > -\frac{1}{G(\mathbf{u})}\frac{\nabla G(\mathbf{u}).\mathbf{u}}{\|\nabla G(\mathbf{u})\|^2} \tag{18}$$

where $G(\mathbf{u}) \neq 0$.

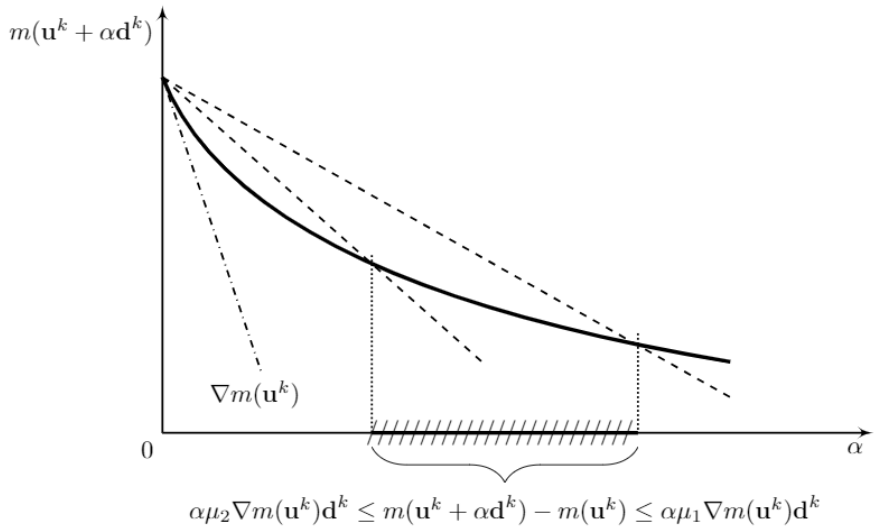

Figure 4: Goldstein-Armijo line search method

Imposing this condition in Eq. (17) only may lead to a very small step α^k and then a poor algorithm performance. It is therefore recommended to use this condition with a step adjustment algorithm in order to conserve a reasonable step length (Santos et al. (2012); Lemaire (2013)). One solution is to use the Goldstein-Armijo (GA) rule (see Figure 4 , Nocedal and Wright (2006)):

$$\alpha\mu_2\nabla m(\mathbf{u}^k)\mathbf{d}^k \leq m(\mathbf{u}^k + \alpha\mathbf{d}^k) - m(\mathbf{u}^k) \leq \alpha\mu_1\nabla m(\mathbf{u}^k)\mathbf{d}^k \tag{19}$$

with

$$\nabla m(\mathbf{u}^k) = \mathbf{u}^k + c^k G(\mathbf{u}^k)\nabla G(\mathbf{u}^k) \tag{20}$$

where $0 < \mu_1 < \mu_2 < 1$. This search rule has the advantage of not requiring any gradient computation. The MHLGA algorithm can be presented as follows:

(MHLGA): Modified Hasofer and Lind with Goldstein-Armijo search

Inputs: Initial solution $\mathbf{u}^0$, $k = 0$

Parameters: $A > 0$,$B > 0$, $0 < r_1 < 1$, $r_2 > 1$, $0 < \mu_1 < \mu_2 < 1$

1. Compute limit state function gradient $\nabla G(\mathbf{u}^k)$
2. Compute search direction $\mathbf{d}^k$
3. Compute c^k
   - If $G(\mathbf{u}^k) = 0$ choose $c^k = B$
   - Else $c^k = A \left| \dfrac{1}{G(\mathbf{u}^k)} \dfrac{\nabla G(\mathbf{u}^k)\mathbf{u}^k}{\|\nabla G(\mathbf{u}^k)\|^2} \right|$
4. Line search (start with $\alpha = 1$). While Goldstein-Armijo rule is not satisfied:
   - If $m(\mathbf{u}^k + \alpha\mathbf{d}^k) - m(\mathbf{u}^k) > \alpha\mu_1 \nabla m(\mathbf{u}^k).\mathbf{d}^k$:

     $\alpha = r_1\alpha$
   - Elseif $\alpha\mu_2 \nabla m(\mathbf{u}^k).\mathbf{d}^k > m(\mathbf{u}^k + \alpha\mathbf{d}^k) - m(\mathbf{u}^k)$:

     $\alpha = r_2\alpha$
5. $\alpha^k = \alpha$
6. $\mathbf{u}^{k+1} = \mathbf{u}^k + \alpha^k\mathbf{d}^k$
7. $\beta = \left\|\mathbf{u}^{k+1}\right\|$
8. $k = k + 1$
9. Check stopping criterion Eq. (12).

4. Numerical validations

Numerical validation of HOS-NWT was first done for 5 irregular wave conditions consisting of 35 realizations each. The focus was on comparing the wave spectrum and main spectral parameters estimated with the measurement data to the target values, and analysis of the corresponding wave crest POE curve was also performed. Based on the 35 realization results, for the validation of the FORM calculation algorithm to which HOS-NWT is applied, the geometrical characteristics of the calculated EDW and the POE result of the EDW estimated by the FORM method were discussed.

4.1. Numerical wave tank setup

The reproduction of the wave elevation generated in the experiment was done for cross-validation in a 2D numerical wave tank measuring 35m in length (L_x) and 5m in depth (L_z). It should be noted that the NWT applied is a digital twin of the engineering wave tank at ECN, but with a smaller size in L_x. This is because the reference position x_0 we target is 18.2m from the wave maker, so a shorter numerical tank is implemented to save computational effort; this modification does not affect the result. The main parameters are listed in Table 1. All the parameters listed in the table are applied to the irregular wave as well as to the EDW wave calculation.

N_x and N_z correspond to the number of modes on the free surface and the wavemaker respectively. The number of decomposed spectral components is decided based on the specified number of points (modes) in the physical domain. N_x is related to the maximum wave number, $k_{max} = N_x\pi/L_x$, and the number of modes in x was chosen based on a constant ratio of $k_{max}/k_p = 15$ providing effective and stable resolution for the whole energetic range of frequency $f < 2.5f_p$. The resolution of wave evolution in time is conducted by applying an adaptive 4th order Runge-Kutta

Table 1: Numerical wave tank setup

Parameter	**Value**
x_0	18.2m
N_x	230
N_z	17
k_{max}/k_p	15
M	5
Tolerance	10^{-4}
$f_{sampling}$	20Hz

Cash-Karp scheme with a time tolerance of 10^{-4}. The non-linearity order M relative to series expansion in wave steepness is set to 5. The numerical simulation is performed with a sampling rate of 20Hz ($f_{sampling}/f_p = 40$). Further details can be found in Ducrozet et al. (2012) and Bonnefoy et al. (2010).

4.2. Test cases

4.2.1. Irregular wave (IW) case

As listed in Table 2, five sea states defined by the JONSWAP spectrum were considered for the irregular wave conditions with $H_s(T_p)$ ranging from 6m(12.3s) to 17m(15.5s). Note that all the cases referred to as SS6 to SS17 were simulated on a scale of 1:65 and all the results were presented as dimensionless quantities or as model scale quantities. 35 realizations were simulated in the numerical wave tank (HOS-NWT) for each sea state, and the ensemble of realizations was then used as a reference for the EDW case in statistical analysis. The simulation time of each single run was 1200s and the length of the time window for the analysis was 1080s (2h40 full scale). By considering the travel time of the shortest wave component $3.5f_p$ at the target position x_0 based on x_0/c_g (c_g being the group velocity), fully developed wave elevation data without any transient period were used in the post-processing

analysis for each sea state.

Table 2: Description of irregular sea state cases (full scale)

Case	H_s **(m)**	T_p **(s)**	γ	**Number of realization** EXP	HOS	**Remark**
SS6	6.0	12.2	1.0	8	35	No breaking wave
SS8	8.3	14.0	1.5	12	35	Breaking waves
SS10	10.0	14.0	1.5	10	35	Breaking waves
SS12	12.0	14.0	1.5	8	35	Breaking waves
SS17	17.0	15.5	2.6	12	35	Breaking waves

4.2.2. EDW case

Each irregular wave case is associated with 3 individual FORM-based EDW cases with different POE, and all EDW cases are calculated to have a target crest C_{target} at $x_0 = 18.2m$ from the wavemaker at $t_0 = 45s$. The target crest C_{target} of each EDW case corresponding to a certain POE level is selected based on the Forristall distribution of each sea state as described in Table 3. As the frequency range considered for the EDW spectrum ranges from $2.2rad/s$ to $10rad/s$, the target time $t_0 = 45s$ is decided based on the travel time of the highest frequency component ($10rad/s$) to the target location 18.2m ($x_0/c_g = 37.2s$). Under the given condition, the spectrum is discretized into $N = 78$ components ($d\omega = 0.1rad/s$) so as to have a repeat period longer than $t_0 = 45s$. The corresponding repeat period is $2\pi/d\omega = 62.83s$ (about 506s in full scale), thus the repetition of the EDW time series before the target time $t_0 = 45s$ can be avoided. Hence, with the given discretized wave components, the EDW elevation can be generated at the wavemaker in a calm water condition and will reach the target location without any disturbance by repeated waves. According to the previous sensitivity study on the number of frequency components by Ghadirian

et al. (2017), $N = 78$ is sufficiently large enough to give a highly accurate resolution for EDW elevation.

Table 3: Description of EDW cases of each sea state (1/65 scale)

Case		H_s (m)	T_p (s)	Target POE	C_{target} (m)	t_0 (s)	x_0 (m)
	SS6-1			10^{-1}	0.0523		
SS6	**SS6-2**	0.092	1.519	10^{-2}	0.0753		
	SS6-3			5×10^{-3}	0.0810		
	SS8-1			10^{-1}	0.0724		
SS8	**SS8-2**	0.128	1.736	10^{-2}	0.1042		
	SS8-3			5×10^{-3}	0.1121		
	SS10-1			10^{-1}	0.0882		
SS10	**SS10-2**	0.154	1.736	10^{-2}	0.1274	18.2	45
	SS10-3			5×10^{-3}	0.1372		
	SS12-1			10^{-1}	0.1073		
SS12	**SS12-2**	0.185	1.736	10^{-2}	0.1557		
	SS12-3			5×10^{-3}	0.1675		
	SS17-1			10^{-1}	0.1530		
SS17	**SS17-2**	0.262	1.923	10^{-2}	0.2223		
	SS17-3			5×10^{-3}	0.2398		

4.3. Numerical simulation results

Figures 5-9 show the estimated wave spectrum and the corresponding wave crest POE curve results at the target position for given sea states. The wave spectrum plotted is the average of 35 numerically calibrated realizations and is compared with the target JONSWAP wave spectrum. Spectrum results are displayed as dimensionless quantities with their corresponding target values. The estimation of the wave spectrum is carried out with the Welch's overlapped segment averaging estimator with time windows of $50T_p \times$ data sampling rate (20Hz) and 50% overlap. The estimated power spectral density of most of the frequency components visually shows comparable results to the target spectrum, but some differences are observed in the

range over $1.2f_p$. The discrepancy near $f/f_p = 1$ appears to increase as the sea condition becomes severe. The main parameters of the wave spectrum for each sea state are listed in Table 4. The maximum differences in significant wave height and peak period are found to be (4.8%) and (1.3%) in SS17 respectively, while T_z (4.8%) and T_1 (4.6%) are observed in SS6, the mildest sea condition.

Table 4: The ratio of the calculated main parameters to target values

	$\frac{H_{s_{HOS}}}{H_{s_{target}}}$	$\frac{T_{p_{HOS}}}{T_{p_{target}}}$	$\frac{T_{z_{HOS}}}{T_{z_{target}}}$	$\frac{T_{1_{HOS}}}{T_{1_{target}}}$	**Kurtosis**	**Skewness**
SS6	+1.8%	+1.1%	-4.8%	-4.6%	3,123	0,154
SS8	-2.1%	0.0%	+0.7%	-0.4%	3,140	0,144
SS10	-2.3%	0.0%	-0.9%	-1.4%	3,174	0,179
SS12	-3.0%	0.0%	-2.3%	-2.3%	3,170	0,214
SS17	-5.8%	-1.3%	+0.9%	+0.5%	3,082	0,223

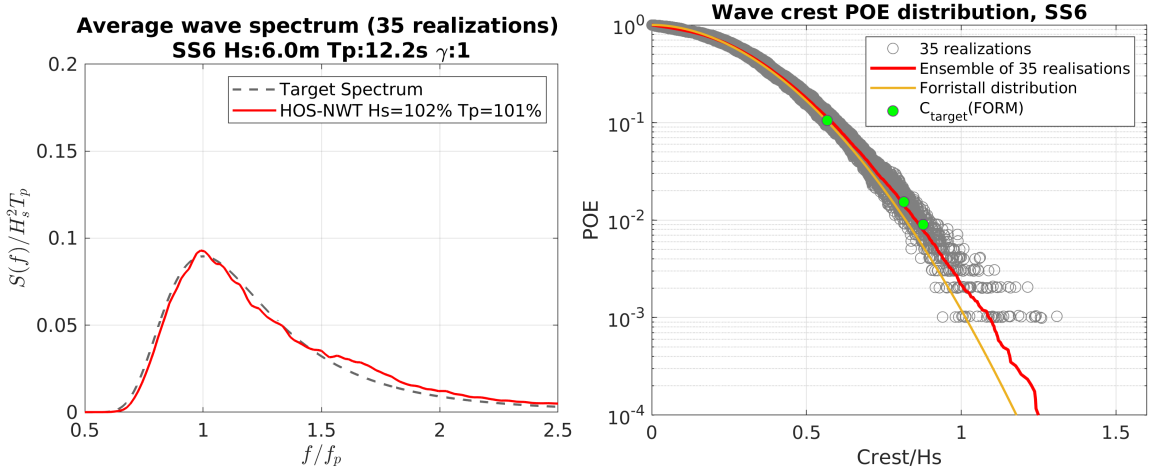

Figure 5: Average wave spectrum of 35 realizations and corresponding wave crest probability distributions, SS6

In each graph, the wave crest exceedance probability (POE) distribution of a given sea state is also presented. Significant wave height in abscissa is expressed

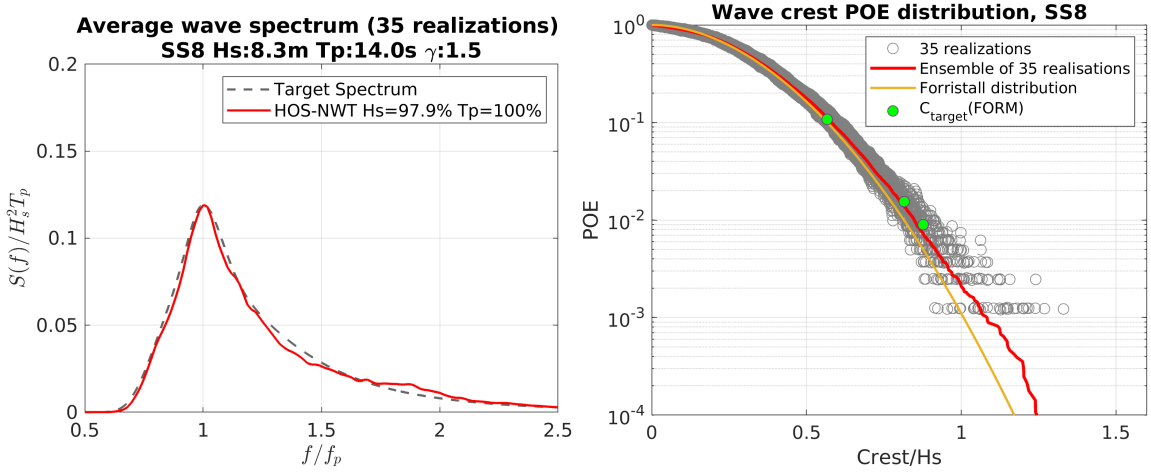

Figure 6: Average wave spectrum of 35 realizations and corresponding wave crest probability distributions, SS8

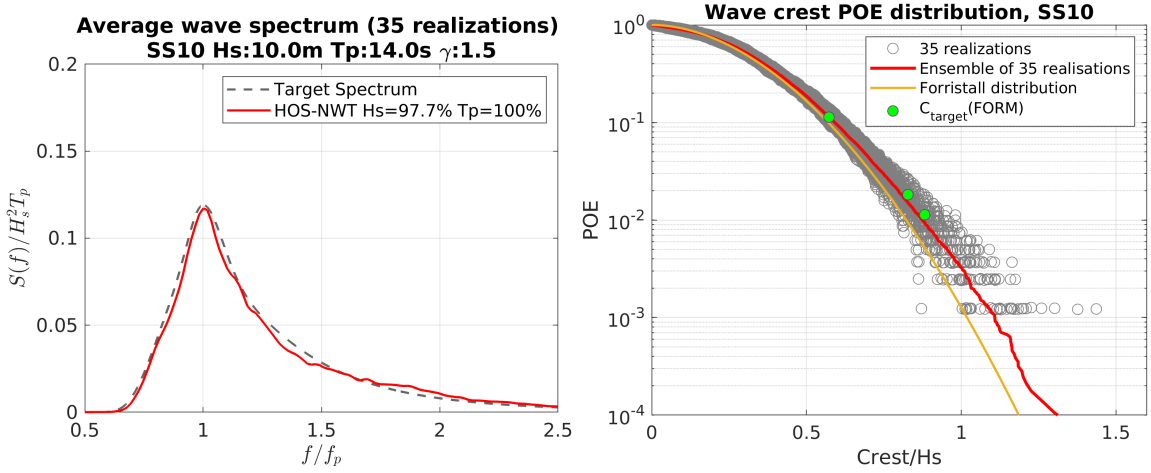

Figure 7: Average wave spectrum of 35 realizations and corresponding wave crest probability distributions, SS10

as a dimensionless quantity with respect to the measured significant wave height. For the comparison with the second-order wave-based Forristall distribution, the POE of a single realization consisting of 35 individual cases (gray markers) and its ensemble (red curve) are plotted together. In most cases, the ensemble POE of all the realizations is distinct from the Forristall distribution (yellow curve), and the gap

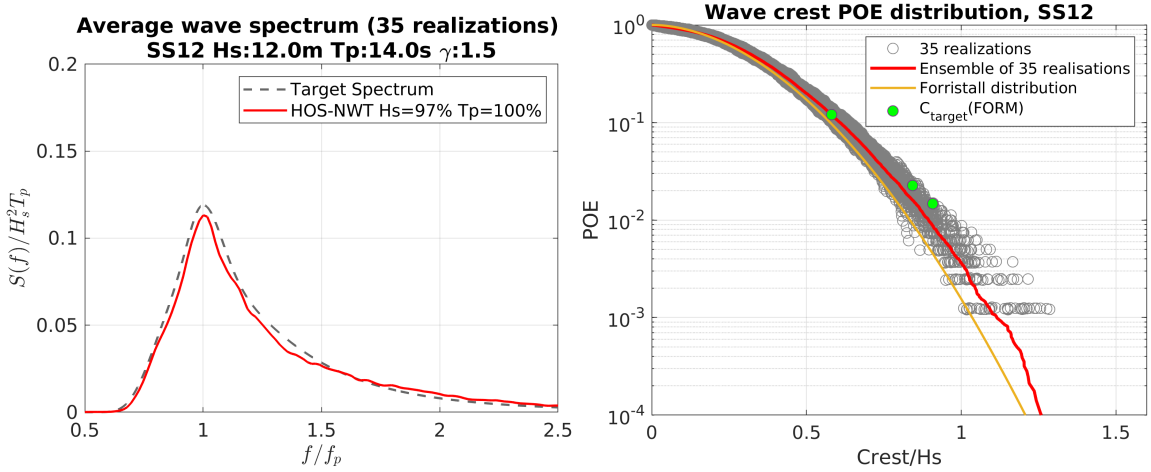

Figure 8: Average wave spectrum of 35 realizations and corresponding wave crest probability distributions, SS12

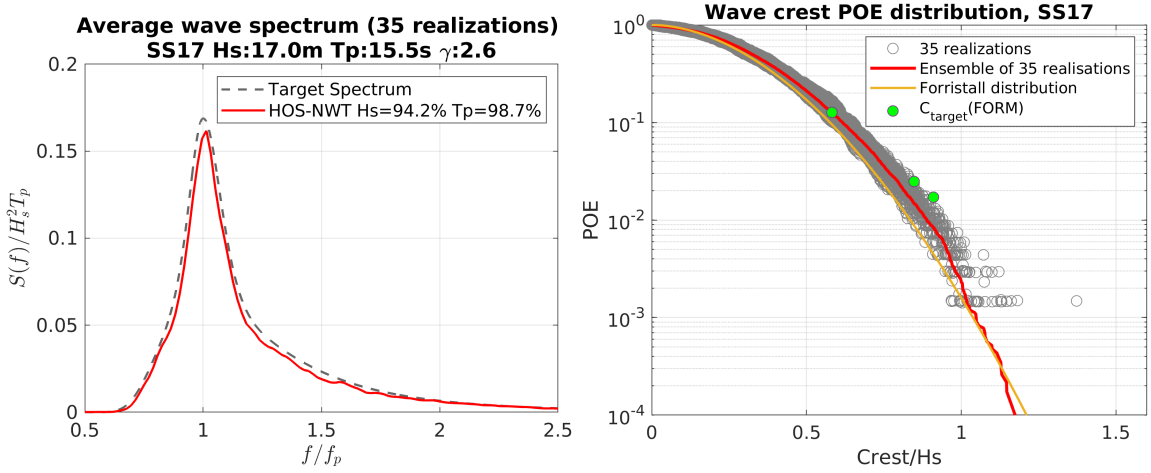

Figure 9: Average wave spectrum of 35 realizations and corresponding wave crest probability distributions, SS17

increases as the POE level decreases. Following Huang and Zhang (2018), it can be said that as the Forristall distribution is derived based on second-order wave theory and HOS-NWT considers higher-order effects responsible for the gap between the ensemble distribution and the Forristall distribution.

The estimation of POE of the target crest C_{target} in a given sea state by the FORM

method was also done and results are represented in the graphs by green points. The estimated POE value using Eq. 10 and 11 with $\mathbf{u}^*$ yielding the target crest C_{target} shows fairly good agreement with the ensemble distribution for 35 realizations in moderate sea states. However, it appears to produce a conservative POE value for C_{target} under harsh wave conditions such as SS12 and SS17.

To find out whether the POE estimation result of the FORM method is related to the sea conditions and characteristics of individual EDWs, the ratio of C_{target} to λ_p of a given sea state corresponding to the crest steepness and the crest error defined as $1 - C_{target}/C_{ensemble}$, were summarized in Figure 10 and Table 5. $C_{ensemble}$ corresponds to the crest value having the POE estimated by FORM on the ensemble POE curve of a given sea state. In other words, it is the crest on the red curve that intersects horizontally with the three green points in Figures 5-9. As shown in Figure 10, it can be seen that the crest error gradually increases as the sea state becomes more severe and the individual EDW becomes steeper, and the trend seems quite clear. In Table 5, which summarizes the same results, when the crest steepness (C_{target}/λ_p) is 2.4% or more, the crest error starts to have a difference of about 5% or more. For cases with C_{target}/λ_p of 3.3% to 4.1% (SS12-2, SS12-3, SS17-2, and SS17-3), the crest error increases at a relatively high rate, from 8.6% to 15.6%. The facts that the energy dissipation mechanisms due to the strong nonlinear phenomena including the breaking waves are expected to be more active as the sea state becomes more severe from SS6 to SS17, and no breaking wave occurred in all EDW cases could be possible reasons for the result. Although it cannot be determined with only one parameter, the relationship between the crest size of individual EDW and λ_p of a given sea state seems to be somewhat related to the FORM POE estimation result.

Since the EDW approach measures and analyzes the response of interest through only one short irregular wave packet, the reality of the calculated EDW remains in

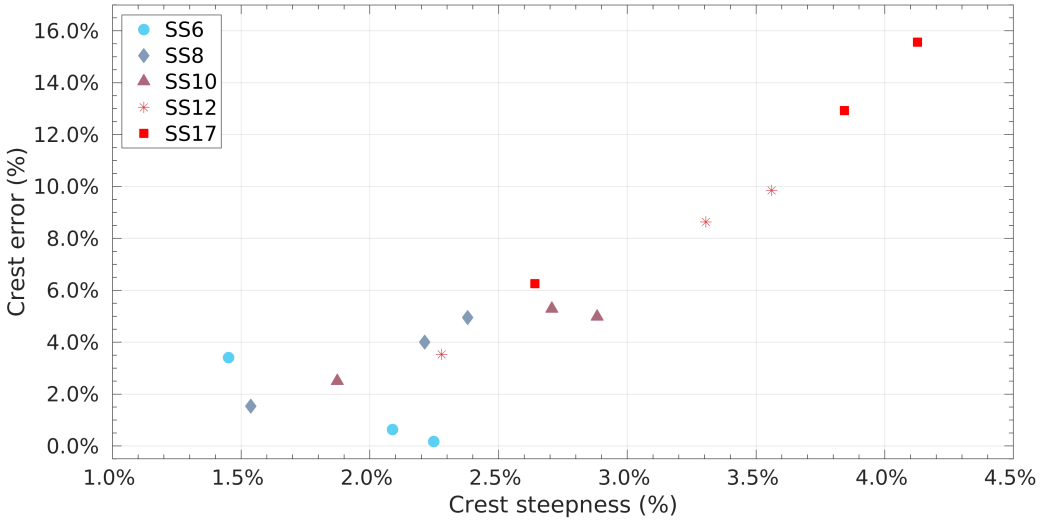

Figure 10: Crest error $(1 - C_{target}/C_{ensemble})$ from the FORM estimation and corresponding crest steepness C_{target}/λ_p for different sea states and POE levels

question and needs to be sufficiently analyzed. Therefore, to check the practicality of the EDW approach, one of the most important objectives is to figure out whether the time series of FORM-based EDW provides the most probable scenario among the waves having a certain crest in a given irregular wave condition. To confirm this, a geometrical similarity review was carried out between the EDW time series and the wave signals of similar magnitude generated in the long-time irregular wave time series.

Each graph in Figures 11 to 15 shows a plot of three EDW time series, along with irregular wave time series containing the target crest of each corresponding EDW case with 2% tolerance. The number of irregular wave events extracted is presented in each graph for reference. The average of all the extracted irregular waves is additionally plotted on each graph to figure out the most probable shape of the irregular time series.

In the case of irregular wave time series extraction, a zero-crossing analysis was

Table 5: Crest error and corresponding crest steepness summary table for different sea states and POE levels

Case		**Crest steepness (%)** C_{target}/λ_p	**Crest error (%)** $1 - C_{target}/C_{ensemble}$
SS6	**SS6-1**	1,5%	3,4%
	SS6-2	2,1%	0,6%
	SS6-3	2,2%	0,2%
SS8	**SS8-1**	1,5%	1,5%
	SS8-2	2,2%	4,0%
	SS8-3	2,4%	5,0%
SS10	**SS10-1**	1,9%	2,5%
	SS10-2	2,7%	5,3%
	SS10-3	2,9%	5,0%
SS12	**SS12-1**	2,3%	3,5%
	SS12-2	**3,3%**	**8,6%**
	SS12-3	**3,6%**	**9,9%**
SS17	**SS17-1**	2,6%	6,3%
	SS17-2	**3,8%**	**12,9%**
	SS17-3	**4,1%**	**15,6%**

performed on 35 realizations for each sea state to list crest events and their occurrence times first. From the list of all events, crests corresponding to the $\pm 2\%$ range of the EDW target crest C_{target} and corresponding time of occurrence are extracted. Based on the crest occurrence time, data covering 1.8s before and after were finally extracted and plotted. For reference, a period of 3.6s was selected based on the SS17-3, which has the longest period.

Looking at the results for each sea state, it is visually observed that various irregular waves are extracted in terms of period and steepness in the case with a high POE level (SS-1 cases in each sea state), and irregular waves similar to the EDW wave time series are extracted as the POE level is lowered from SS-1 to SS-3

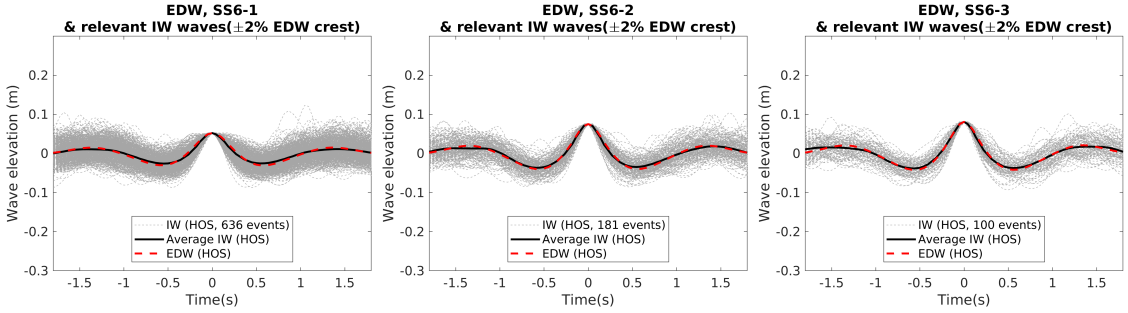

Figure 11: EDW time signal shape comparison with all corresponding waves from irregular sea state, SS6 (model scale)

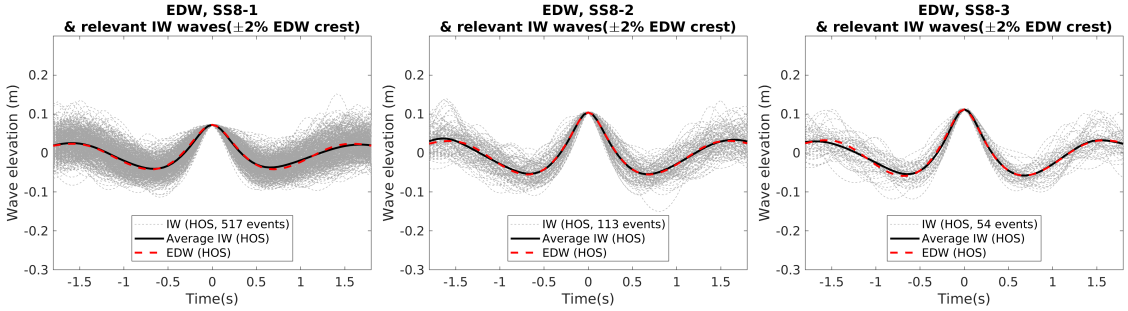

Figure 12: EDW time signal shape comparison with all corresponding waves from irregular sea state, SS8 (model scale)

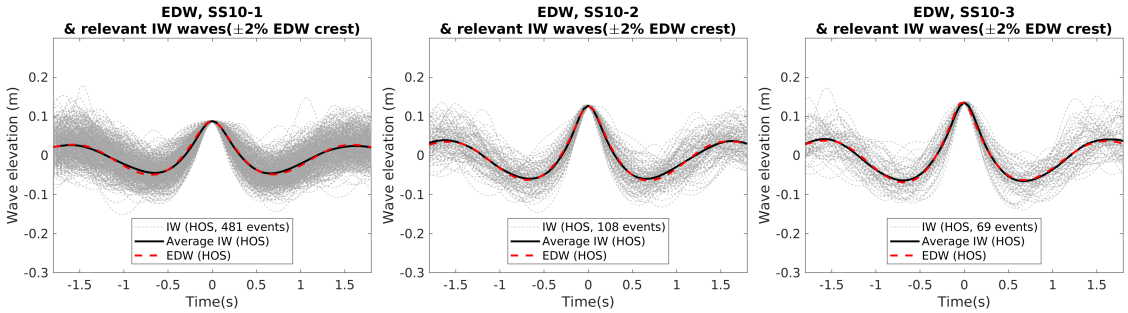

Figure 13: EDW time signal shape comparison with all corresponding waves from irregular sea state, SS10 (model scale)

in each sea state. Although this may appear relatively similar because the number of events corresponding to the target is quantitatively small as the POE level is lowered, it can be seen that from a qualitative point of view the individual waves extracted

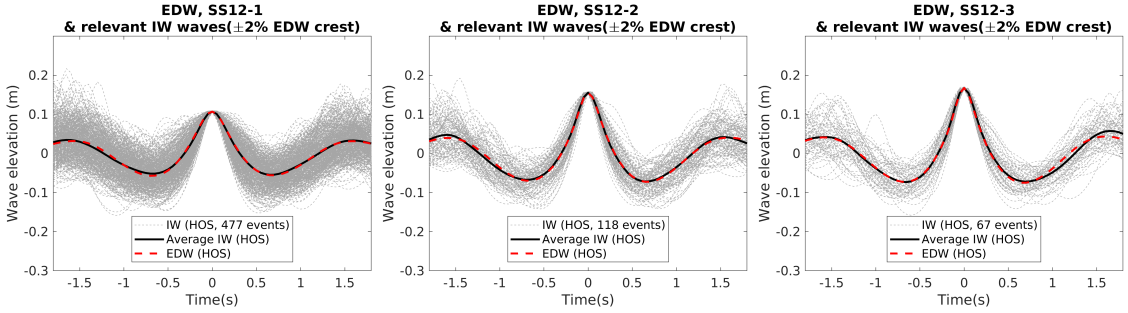

Figure 14: EDW time signal shape comparison with all corresponding waves from irregular sea state, SS12 (model scale)

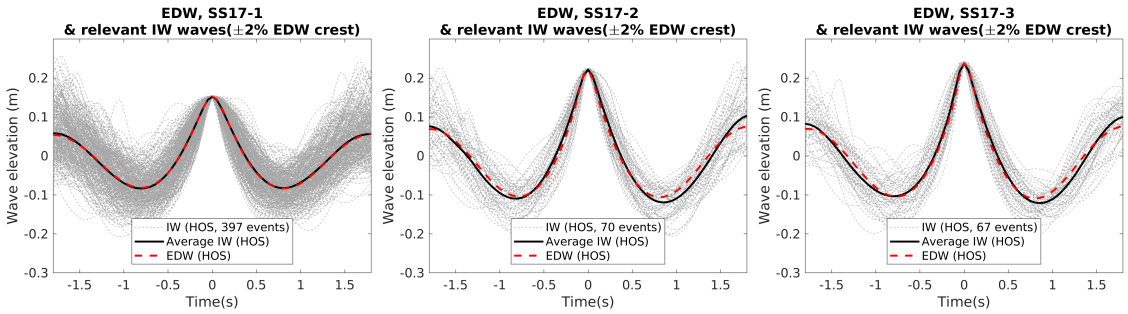

Figure 15: EDW time signal shape comparison with all corresponding waves from irregular sea state, SS17 (model scale)

are basically similar in shape to the EDW wave.

It is noteworthy that the average wave profile of the irregular wave has a very similar shape to the EDW wave profile in all cases regardless of the POE level, while some discrepancies are found in the size of the trough and crest around the focusing point in the EDW case of SS17, the most severe case. Nevertheless, it can be said that the FORM-based EDW calculation process applying HOS-NWT provides the most probable nonlinear wave shape considering that the overall shape does not deviate significantly from the qualitative aspects compared to the average shape of extracted nonlinear irregular waves.

A similar result was observed in previous research by Fedele et al. (2017). They

conducted a long-time simulation of a particular storm-generated sea state with a Higher-Order Spectral (HOS) method and compared its crest statistics with results from analytical probability models. They found that a model called Fedele's Space-Time stochastic (FST) considering the wave effect up to a third order had a good match with the HOS result. They also investigated a rogue wave of crest/H=1.6 in terms of shape and occurrence probability in a given sea state and found that the shape is fairly similar to those observed in different storm seas namely Andrea, Draupner, and Killard, meaning that rogue waves are generated with a similar mechanism.

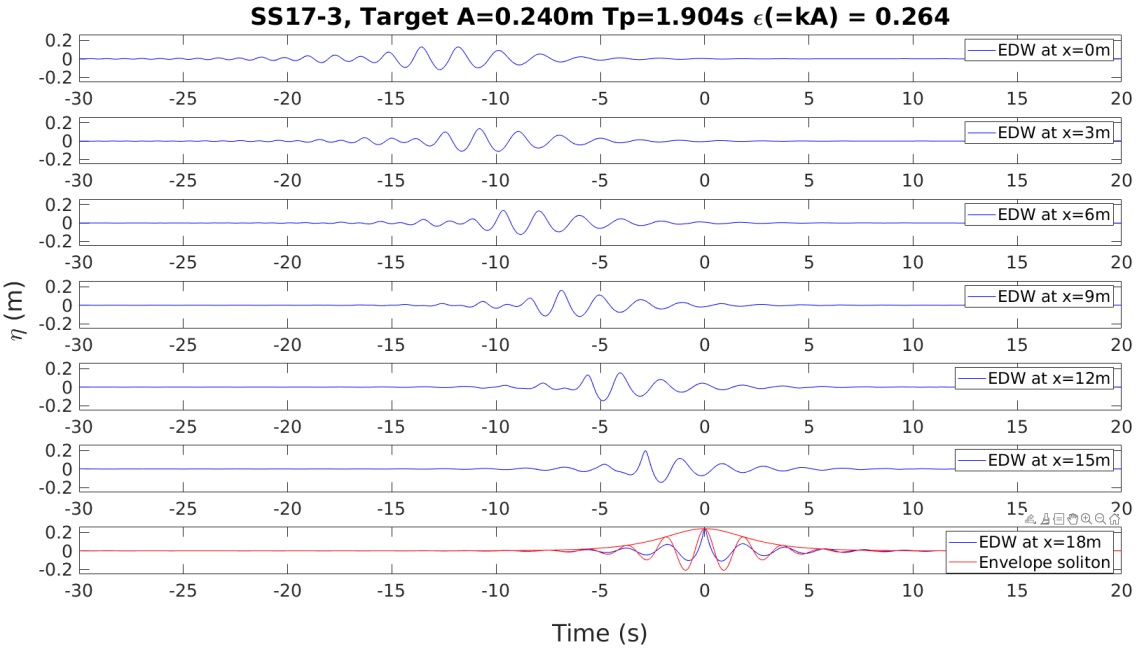

Figure 16: Evolution of the EDW profile from the wavemaker (0m) to the target position (18m) having a desired profile with a specified target amplitude (blue curve) and envelope soliton (red curve). Both were calculated with the same input parameters: A =0.238m, T_p =1.904s, and $\epsilon = kA$ =0.264)

Previous research by Klein et al. (2021) investigated the applicability of envelope soliton (ES) for the analysis of wave-structure interaction. ES was generated and

compared with a standard MLRW profile using a simple linear model for wave and response descriptions. They found that the shape of ES is fairly similar to the MLRW profile. Following this research, we compared the FORM-based EDW with an ES exhibiting the same amplitude and frequency, see Figure 16. We observe that the FORM-based EDW results in a wave packet at the target location, which can only be approximated roughly by an ES. In addition, this wave packet experiences highly unsteady features between its generation and the target location. On this ground, in our specific application, the ES does not seem adequate to replace the EDW procedure.

The work of Klein et al. (2021) calculated the ES and EDW yielding a specified vertical bending moment (VBM), while this study considers crest amplitude as a target value for the calculation of ES and EDW. Complementary, their approach was limited to a linear model, while the present FORM-based procedure considers a fully nonlinear wave model in the EDW calculation. Those elements may explain the different conclusions on the possible use of the ES as a design wave.

Another argument for the use of the ES in Klein et al. (2021) is that it is almost impossible to reproduce the linear wave-based EDW in a wave tank because of the wave nonlinearities. However, in this study, we were able to overcome this limitation by using a nonlinear Numerical Wave Tank (HOS-NWT) in the EDW calculation algorithm.

Figure 17 shows the overall distribution of wave crest and period pair for all waves including EDW. Each graph corresponds to a different sea state result, and the three separate groups of points in each graph represent the extracted waves based on three different C_{target}. As pointed out earlier, a large dispersion can be observed for the crest and period group having the highest POE level in all sea states, and the degree of dispersion in the period obviously diminishes as the POE level decreases.

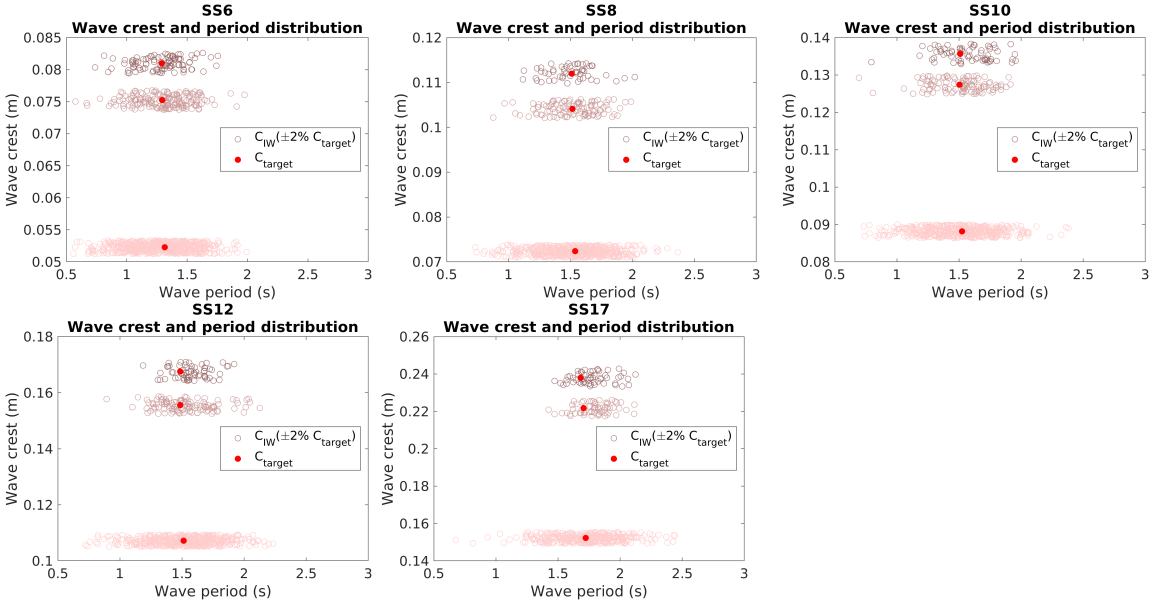

Figure 17: Wave crest and period distribution (model scale)

No noticeable change in the trend of the distribution is observed as the sea state condition changes. In most cases, the crest and period pair of EDW (red points) are located almost at the center of the irregular wave group, implying that the EDW calculated by the FORM method represents the most probable wave profile for a given sea state.

Meanwhile, as observed from the time signal results, the EDW cases with a relatively large discrepancy in shape corresponding to SS17-2 and SS17-3 are somewhat farther from the center of the extracted wave group. From the time signal results in Figure 15, in both cases, the difference in period seems to be mainly caused by the shape of the trough that occurred after the focusing crest, and the shape of the signals generated before the focusing crest is very comparable to the average shape of the irregular waves. Given the above results, it can be considered that the numerical simulation of nonlinear wave elevation with HOS-NWT and the calibration proce-

dure successfully validate the generation of the target sea state and target EDW at the desired position of the numerical wave tank.

5. Experimental study

The wave qualification process was checked by comparing the irregular sea state results in the experiment with those generated in the numerical wave tank. Thus the same wave spectrum data including wave phase information used in the numerical simulation were applied as an input in order to perform cross-validation and to figure out uncertainties in the experimental setup (wavemaker, wave gauge, and absorbing beach). Note that the experimental study was performed with a reduced number of realizations for the irregular wave cases as listed in Table 2, and thus the same number of realizations was considered in the numerical simulation presented in this section.

5.1. Setup and test cases

All the waves were generated on a scale of 1:65 in an ocean engineering tank, 50m long, 30m wide and 5m deep in Ecole Centrale de Nantes, see Figure 18. Several wave gauges are positioned in the tank. The reference position is (18.2m, 15m) expressed in the basin coordinate system, where wave gauge No.2 (WG2) is positioned. Five wave conditions identical to the numerical simulation were tested. Each sea state consists of at least 8 (maximum 12) realizations of 3-hour full-scale wave time series. In each irregular wave case, as mentioned above, the aim of the experimental study was to validate the numerical simulation, thus exactly the same EDW input data were used to generate the calculated EDW elevation at $x_0 = 18.2m$ and $t_0 = 45s$ (see Table 3).

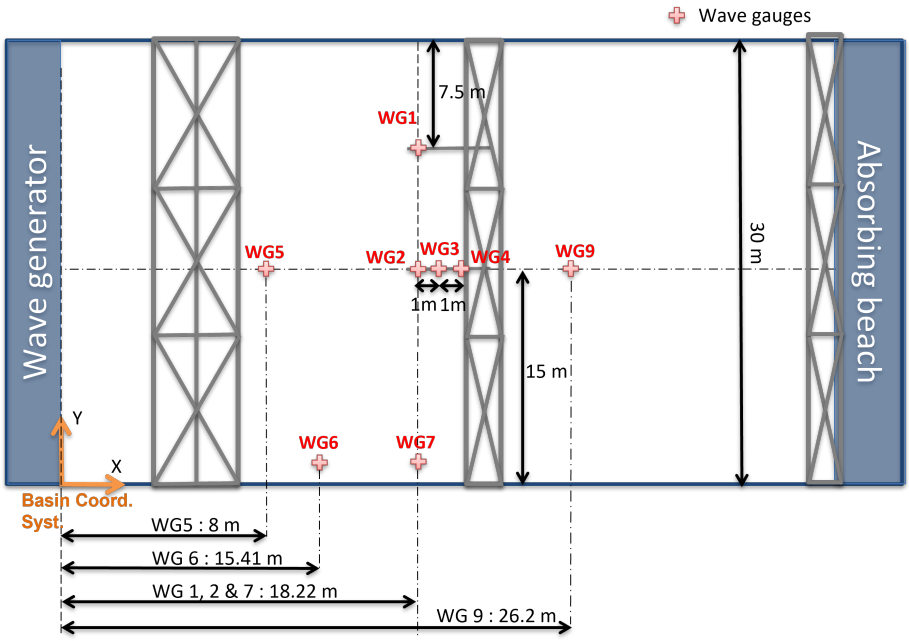

Figure 18: Experimental setup

5.2. Irregular wave results

The power spectral density of each sea state was estimated using Welch's overlapped segment averaging estimator following the numerical simulation. Data measurement was done with a sampling rate of 200Hz, and post-processing was carried out with the data of wave gauge No.2 installed 18.2m from the wavemaker which corresponds to the target position x_0 (see Figure 18). Figures 19-23 show the estimated average wave spectrum of the specified realizations for each sea state and ensemble probability distribution of wave crest at the target position.

As shown in the figures, the spectrum results of the experiment and the numerical simulation are overall consistent, but we observed that there were some differences in size and change pattern of the spectrum curve in specific frequency ranges. The experimental wave spectrum tends to have a larger energy density in the higher

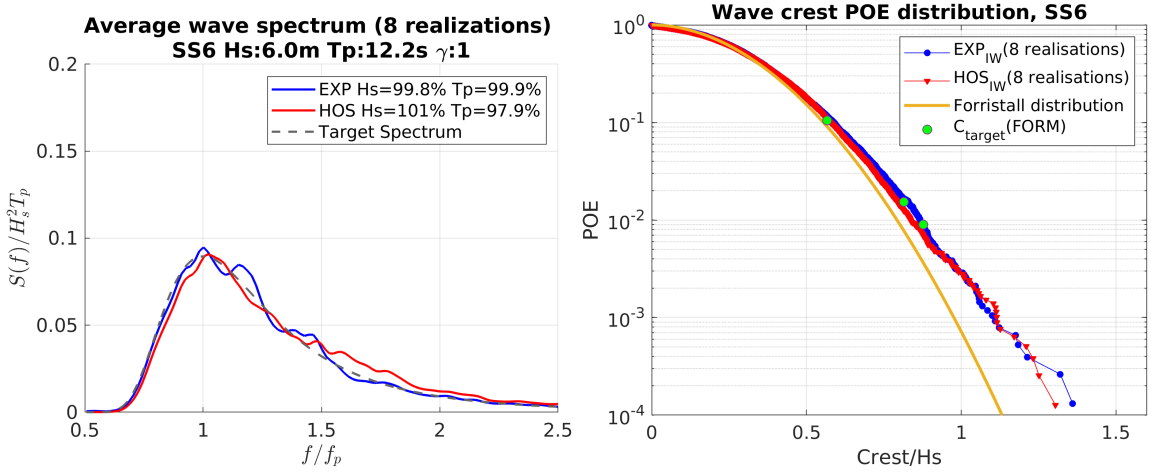

Figure 19: SS6, Comparison of measured and calculated average wave spectrum of 8 realizations and corresponding wave crest probability distributions

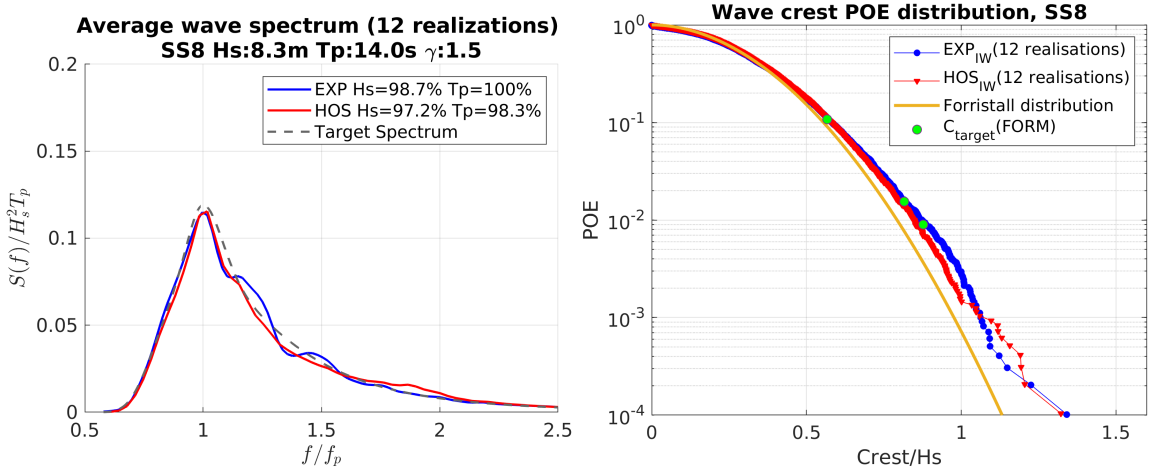

Figure 20: SS8, Comparison of measured and calculated average wave spectrum of 12 realizations and corresponding wave crest probability distributions

frequency range than the numerical results. Most of the discrepancies appear to come from frequency components higher than $f/f_p = 1.0$. The local variation of the numerical results is relatively small compared to the experiment, and the overall shape was found to be more convergent to the target spectrum. The estimated spectrum parameters H_s and T_p both show good agreement with the target values,

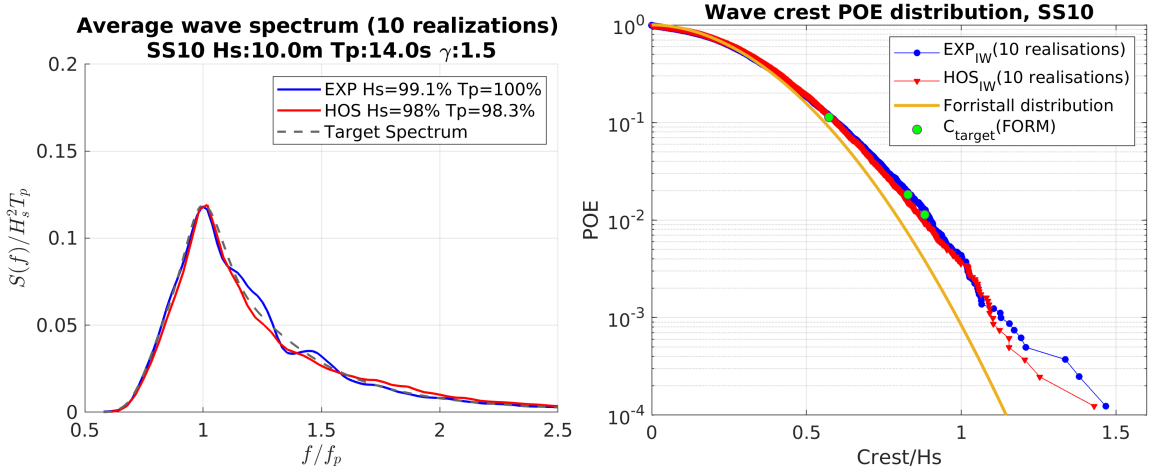

Figure 21: SS10, Comparison of measured and calculated average wave spectrum of 10 realizations and corresponding wave crest probability distributions

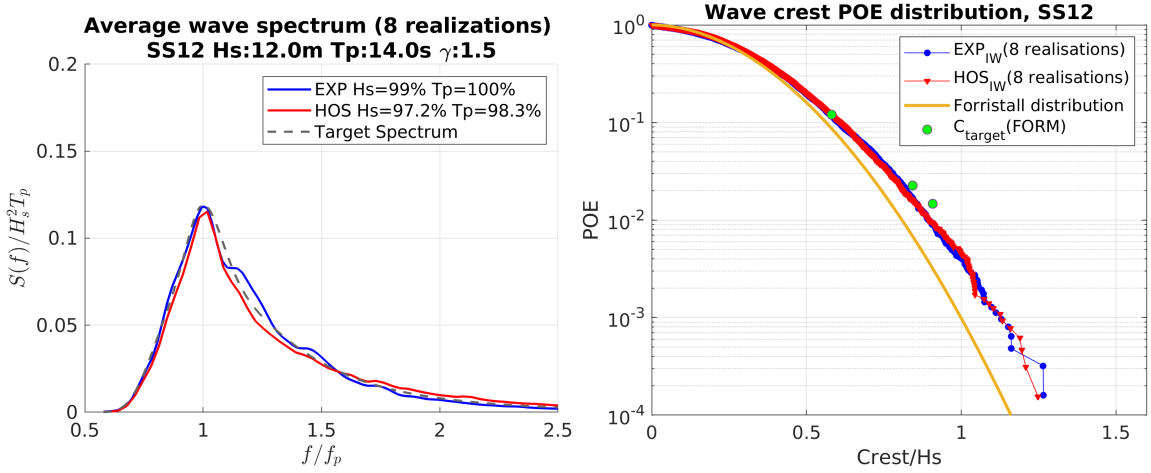

Figure 22: SS12, Comparison of measured and calculated average wave spectrum of 8 realizations and corresponding wave crest probability distributions

and as expected, SS17 has the largest difference in H_s with respect to the target in both experiment (1.3%) and numerical simulation (5.5%). Regarding the difference in T_p, no significant discrepancy was found over all cases. The estimated T_p of both experiment and numerical result is over 97.9% of the target T_p.

The aforementioned discrepancy between experiment and calculation in wave

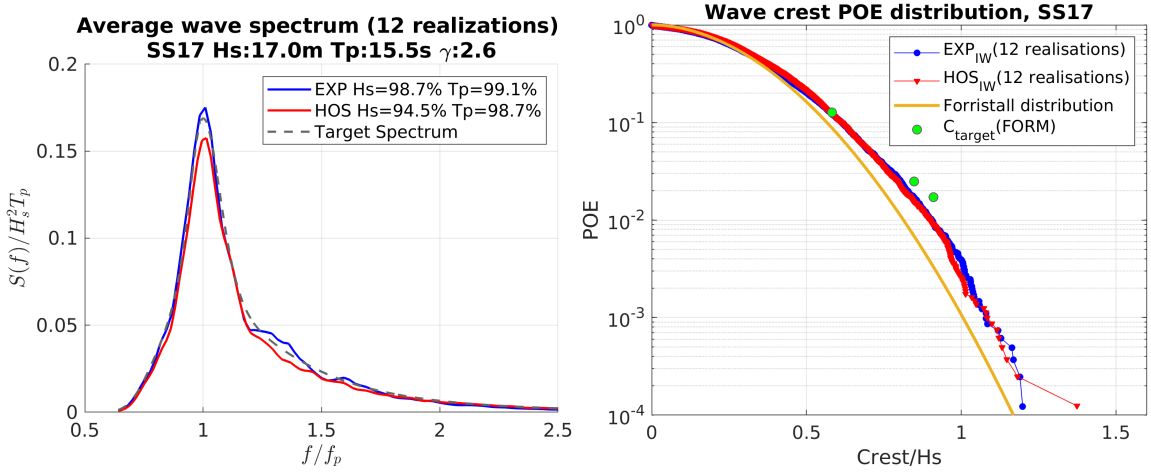

Figure 23: SS17, Comparison of measured and calculated average wave spectrum of 12 realizations and corresponding wave crest probability distributions

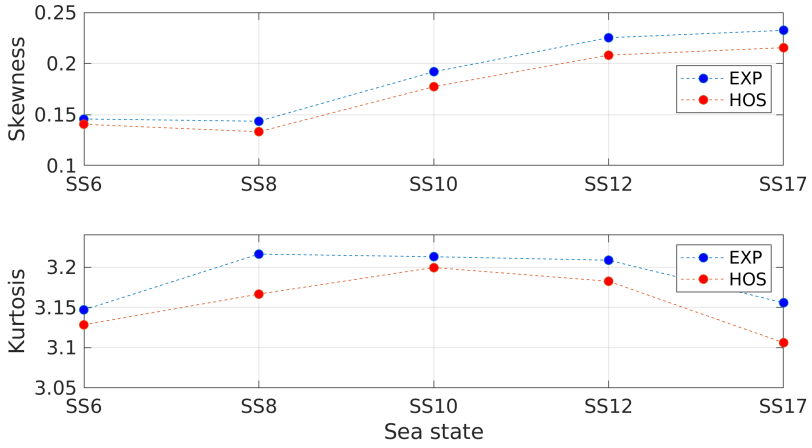

Figure 24: Changes in Skewness and Kurtosis by sea state

spectrum also naturally affects the POE curve as well. As the estimated spectrum of the experiment has larger energy in the high-frequency range, this results in a higher crest distribution, reducing the experimental slope in the POE curve. Compared with the numerically calculated wave crest POE curve with 35 realizations (Figures 5-9), which can be considered more statistically converged, a slight difference is also observed in each sea state. Nevertheless, overall, the two measured and calculated

POE curves up to $Crest/Hs = 1$, which corresponds to around the POE of 4×10^{-3} in each sea state, appear to agree fairly well with each other. As mentioned in the numerical analysis results in section 4.3, the theoretical Forristall distribution has a different trend in slope, showing that the curve is always steeper than the other empirical POE distributions in all sea states as the higher-order effects above second-order are omitted. In the SS17 case which shows the greatest difference with the target spectrum, it is found that the lower the POE level, the closer the ensemble distribution is to the Forristall distribution.

The C_{target} plotted on the estimated POE with Eq. (10) and (11) is placed nearly on the ensemble POE distribution in the relatively moderate sea states. As the sea state becomes severe (SS12 and SS17 cases), however, the POE estimated by FORM tends to give a conservative value. Jensen (2009) likewise found that FORM calculated a smaller β_{FORM} than brute force wave simulations. Although the POE analytically estimated by FORM tends to move vertically upward in the severe wave cases, each result can be viewed as a possible scenario as it is still within the range of the single probability distribution group.

Figure 24 shows the skewness and kurtosis distribution of experiments and numerical analysis for each sea state. The skewness, which represents the asymmetry of the free surface profile corresponding to the second-order effect, increases as the sea state became severe. This confirms that steep waves occur more frequently in severe conditions as expected. The largest difference in skewness is found in the most severe sea state, SS17. The kurtosis of most sea state cases is in the range from 3.1 to 3.2 (Gaussian process=3), and a tendency for kurtosis to gradually decrease in severe conditions is observed. SS17 shows the biggest difference between numerical and experimental results. Given that SS17 has the highest skewness, strong nonlinear effects and energy dissipation mechanisms may induce a large discrepancy in

the spectrum results, which in turn leads to the largest differences in skewness and kurtosis.

Considering that the same input was used in the two environments, the numerical and the physical wave tank, there are some factors that affect the wave quality in each condition. From an experimental point of view, the most probable reasons for this variability are: i) the decrease in measurement accuracy of the resistive wave gauge due to temperature change and impurity adhesion, ii) three-dimensional effects of the wave tank such as the occurrence of transverse modes related to the discontinuous wavemaker flaps, iii) reflected wave due to the imperfection of the absorbing beach, and iv) residual waves from the previous test case. However, as the wave quality varies depending on the condition of the reference tank, and wave evolution at various locations along the tank is also significantly different, further studies on the wave tank are needed to quantify the factors mentioned in this regard.

In the case of the numerical wave tank, since the wave breaking model is applied to most of the sea states except the mildest one (SS6), the modeling of sea states including wave breaking phenomena is likely to cause such discrepancies. According to the previous research by Seiffert and Ducrozet (2018), who carried out a comparative study of measured and calculated breaking waves, energy loss induced by wave breaking phenomena is mostly observed in the higher frequency range over $f/f_p = 1$, while little energy loss is seen in the lower frequency range. The study also focused on the possible causes of the discrepancy between measured and calculated breaking waves and mentioned that the process of gradually reducing the energy before the wave overturns for numerical stability is one possible reason why the calculated wave may produce less energy than measured in the breaking region.

As the numerical wave tank considers only the main characteristics of the physical wave tank in a large framework excluding the uncertain factors mentioned, some

local differences in wave spectrum results are attributed to the causes. However, the overall trends agree well with each other. In addition, based on the POE distribution results and the changing trend of the parameters (kurtosis and skewness) of all the cases, it can be said that the HOS-NWT is capable of accurately generating strong nonlinear wave elevations.

5.3. EDW time signal comparison

To check the EDW wave quality, the EDW time signals measured in the experiment were compared with the numerical simulation results. In Figures 25-29, three EDW time signals corresponding to 3 different C_{target} in a given sea state are presented in each figure. The overall shape of the measured EDW time signal matches very well with the numerically calculated time signal in most cases. A slight time shift and differences in magnitude are observed at surrounding waves, but it seems insignificant. The average difference in crest appears to be less than 3% at the focusing point corresponding to $t = 45s$. Target crest C_{target} at t=45s tends to far exceed the neighbor peaks and this trend becomes even clearer as the target POE level decreases from SS-1 to SS-3 in each sea state, see H/λ of all EDW cases in Table 6.

The difference between the C_{target} of each EDW case and the measured crest C_{EXP} is listed in Table 6 for all cases. The steepness and period listed in the table are the values calculated with wave height and period of the EDW at t_0 =45s to characterize each EDW case. In general, the higher the wave slope and the shorter the wave period, the greater the non-linearity of waves, which tends to increase the difference between the peak generated by the actual wavemaker and the theoretical value. An interesting point observed in the EDW case is that the largest difference up to 11.0% between C_{target} and C_{EXP} is mostly observed in the SS6 sea state, the

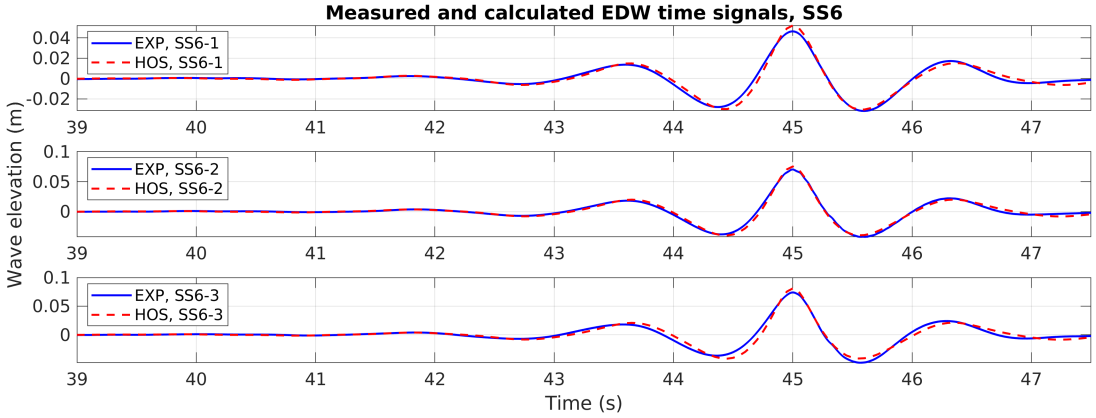

Figure 25: Measured and calculated EDW time signals at x_0 =18.2m, SS6 (model scale)

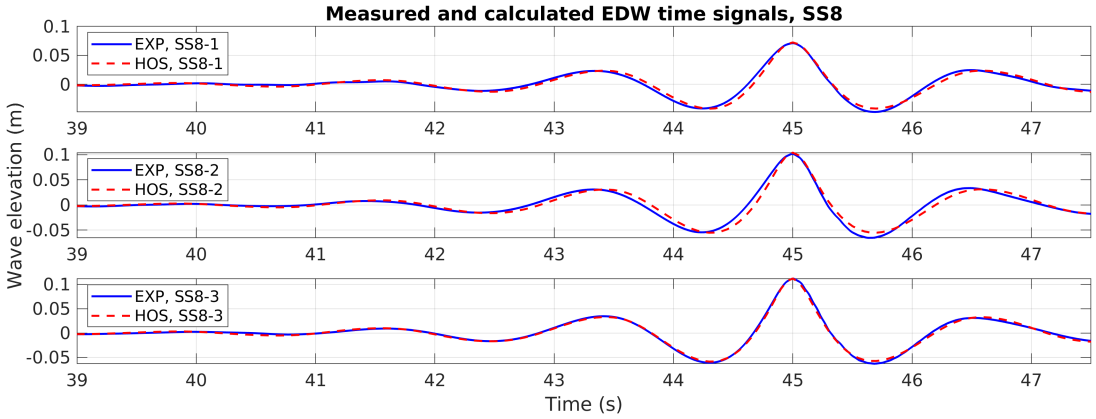

Figure 26: Measured and calculated EDW time signals at x_0 =18.2m, SS8 (model scale)

mildest sea state. Looking at the characteristics of EDW waves of the SS6 condition, the wave steepness of the three cases is the lowest compared to the other EDW cases, while the wave periods of three cases are around 1.3 seconds, which are relatively short compared to the other cases.

However, the period of these cases is not short enough to significantly affect the wave quality when considering the wavemaker performance. Considering that the wave parameter range of the tank that the wavemaker guarantees a good quality wave is 0.5s-5s in wave period and 0%-11% in H/λ, the cause of the discrepancy

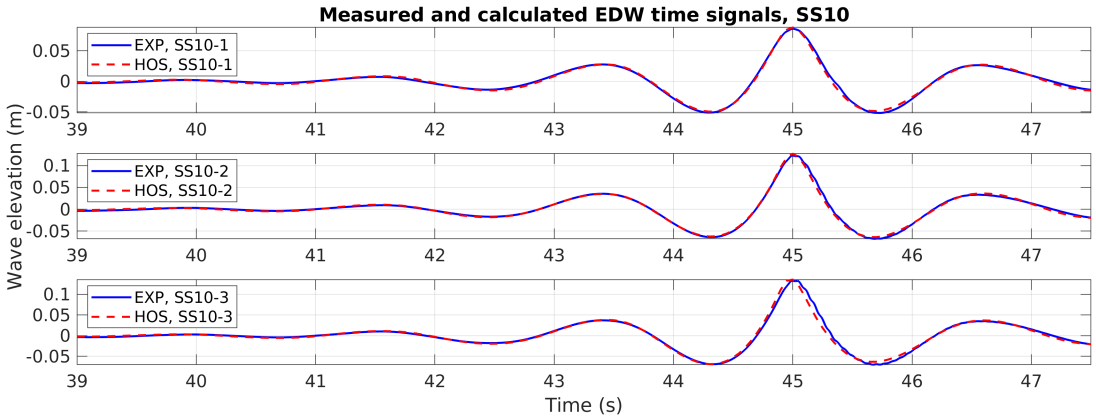

Figure 27: Measured and calculated EDW time signals at x_0 =18.2m, SS10 (model scale)

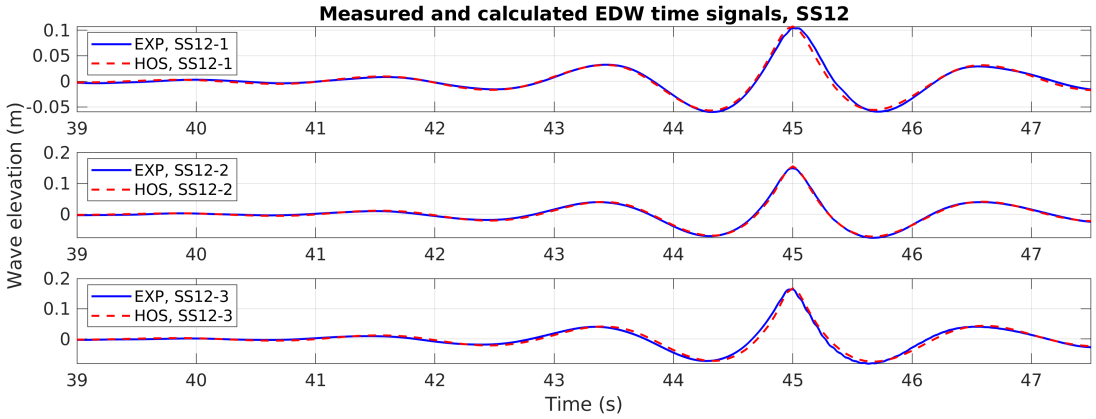

Figure 28: Measured and calculated EDW time signals at x_0 =18.2m, SS12 (model scale)

in the SS6 cases having moderate steepness from 3% to 4.7% cannot be regarded as simply due to the influence of the wave period. In the case of SS17, which has the steepest EDW with H/λ of up to about 7.9% and the longest periods of about 1.72s, the measured C_{EXP} is almost identical to the C_{target}, showing that the wave generation is accurate even for very steep wave fields. From an experimental point of view, given that the largest discrepancy is observed in the EDW having relatively small focusing waves in size, the experimental uncertainties are likely to affect the wave quality the most. In the SS8, SS10, and SS12 cases, which have similar wave

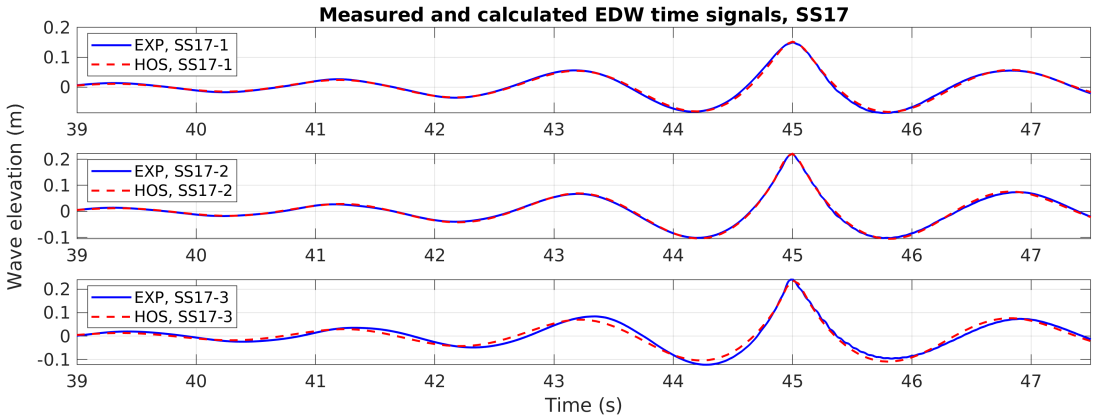

Figure 29: Measured and calculated EDW time signals at x_0 =18.2m, SS17 (model scale)

Table 6: Difference between C_{target} and C_{EXP} of all EDW cases (model scale)

Case		$(\frac{H}{\lambda})_{EDW}$ (%)	T_{EDW} (s)	C_{EXP} (m)	C_{target} (m)	$\frac{C_{EXP}}{C_{target}}$
	SS6-1	3.06	**1.32**	0.0465	0.0523	**0.890**
SS6	**SS6-2**	4.40	**1.30**	0.0704	0.0752	**0.936**
	SS6-3	4.72	**1.29**	0.0740	0.0810	**0.914**
	SS8-1	3.10	1.54	0.0712	0.0724	0.983
SS8	**SS8-2**	4.44	1.52	0.1017	0.1041	0.976
	SS8-3	4.77	1.51	0.1119	0.1120	0.999
	SS10-1	3.77	1.52	0.0862	0.0881	0.978
SS10	**SS10-2**	5.42	1.50	0.1233	0.1274	0.968
	SS10-3	5.58	1.51	0.1329	0.1357	0.979
	SS12-1	4.56	1.51	0.1041	0.1072	0.971
SS12	**SS12-2**	6.63	1.48	0.1492	0.1555	0.959
	SS12-3	7.03	1.49	0.1643	0.1675	0.980
	SS17-1	**5.09**	1.72	0.1497	0.1523	0.983
SS17	**SS17-2**	**7.21**	1.71	0.2207	0.2217	0.995
	SS17-3	**7.85**	1.68	0.2414	0.2380	1.014

periods, no clear trend is found in the relation between steepness and the difference in wave amplitude. In most cases, the measured crest C_{EXP} is smaller than C_{target}

with an average difference of 3.2%.

5.4. Geometrical reviews on EDW wave

Geometrical reviews of the calculated EDW time signal with all the relevant irregular wave signals measured in the experiment were performed. In the same way as the numerical analysis, irregular waves measured in each sea state with ±2% tolerance of C_{target} were extracted and plotted together with the numerically calculated EDW time signal. In addition, the average shape of the irregular waves extracted from the experiment and numerical simulation are presented to see how similar they are to each other and to EDW.

Figures 30-34 show the corresponding results for each sea state. As expected, in all cases without exception, the same trend as that observed in the numerical simulation is confirmed. The shape of the EDW time signal is observed to be very similar to the average time signal of all the extracted irregular waves, while in the SS17-3 case, the EDW wave signal has a relatively different shape in pre- and post-crest at $t = 45s$ compared to the mean wave signal. When all the individual irregular waves extracted with a ±2% tolerance of C_{target} are considered, results show a reasonable trend in terms of the overall shape. Considering the irregular wave itself consisting of numerous harmonic functions, in the case with a high probability of occurrence (SS-1 cases) in each sea state, it is observed that the irregular waves extracted from a sea state have various steepness and wave periods. And as the magnitude of C_{target} increases, the degree of dispersion in wave period and steepness decreases, and thus irregular wave signals which are geometrically more similar to the EDW were extracted.

The corresponding wave crest and period distributions for the measured irregular waves extracted and the EDW are presented in Figure 35. The results are expressed

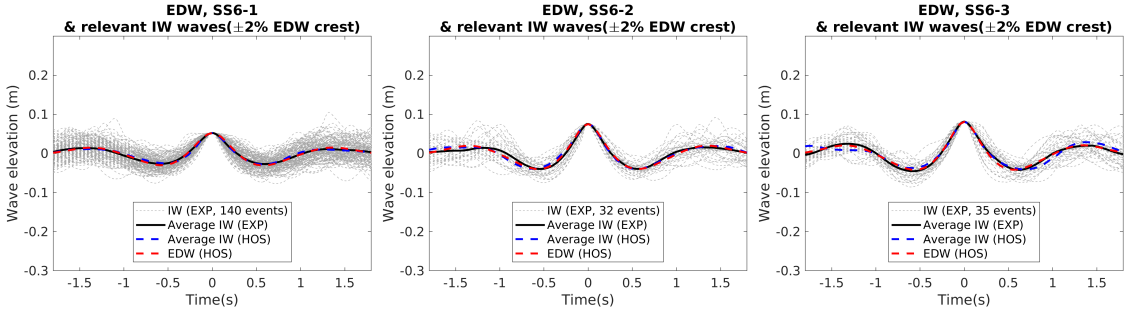

Figure 30: EDW time signal shape comparison with all corresponding waves from irregular sea state, SS6 (model scale)

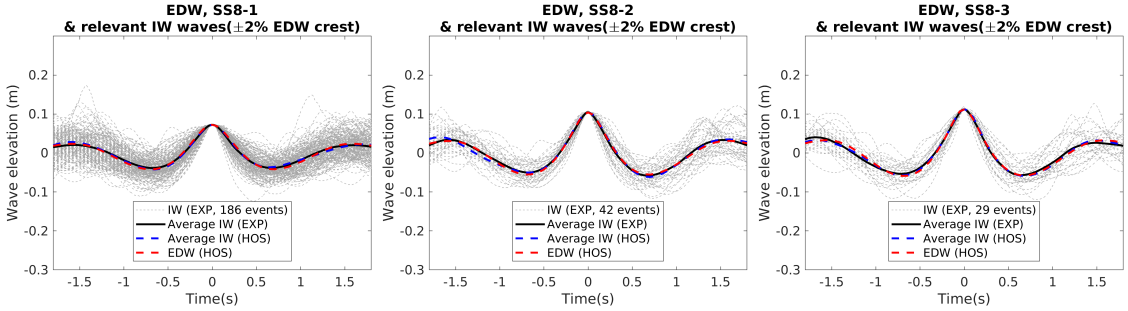

Figure 31: EDW time signal shape comparison with all corresponding waves from irregular sea state, SS8 (model scale)

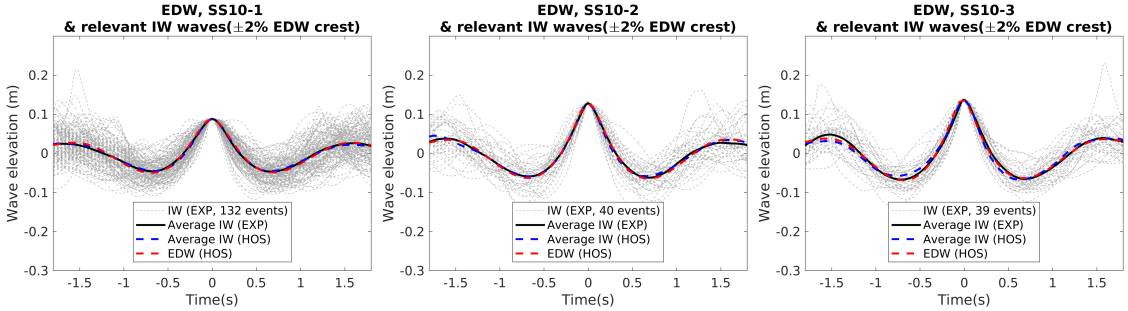

Figure 32: EDW time signal shape comparison with all corresponding waves from irregular sea state, SS10 (model scale)

in the same way as the numerical analysis results in section 4.3. Although some deviation of wave events is found in each case, the crest and period pairs of most waves are in a specific range. As the number of realizations decreases, the waves are

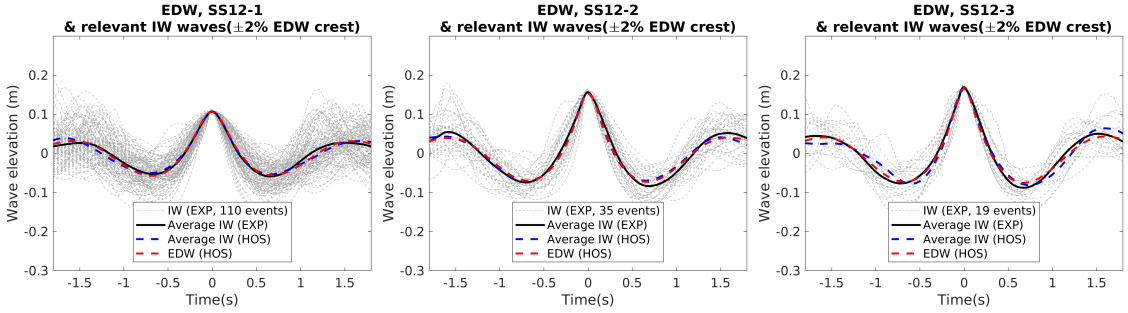

Figure 33: EDW time signal shape comparison with all corresponding waves from irregular sea state, SS12 (model scale)

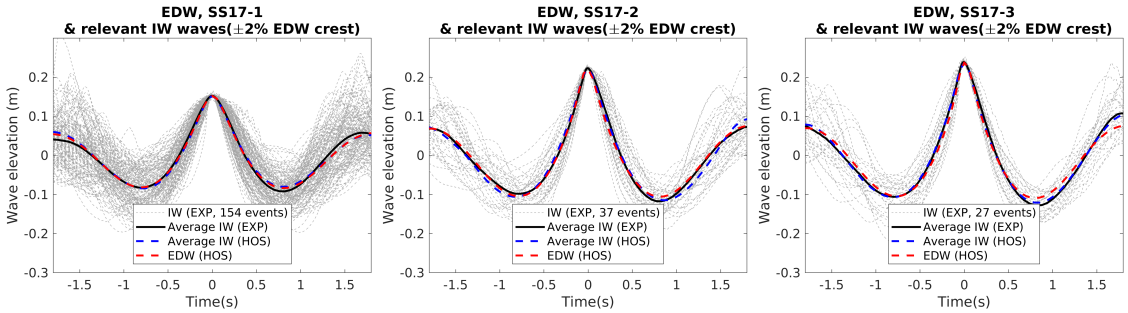

Figure 34: EDW time signal shape comparison with all corresponding waves from irregular sea state, SS17 (model scale)

distributed in a relatively reduced range compared to the numerical analysis which considered 35 realizations for each sea state, and it is found that the EDW is still in a position corresponding to the average in each distribution group. This confirms that the FORM-based EDW wave profile generates a given target crest with the most probable shape. Thus it can be said that the FORM algorithm coupled with HOS-NWT is clearly able to produce the nonlinear focusing wave profile which can occur in a given nonlinear irregular sea state.

6. Conclusion

Overall, through the numerical simulation itself as well as the comparison with experimental results for irregular wave sea states, this study has validated that the

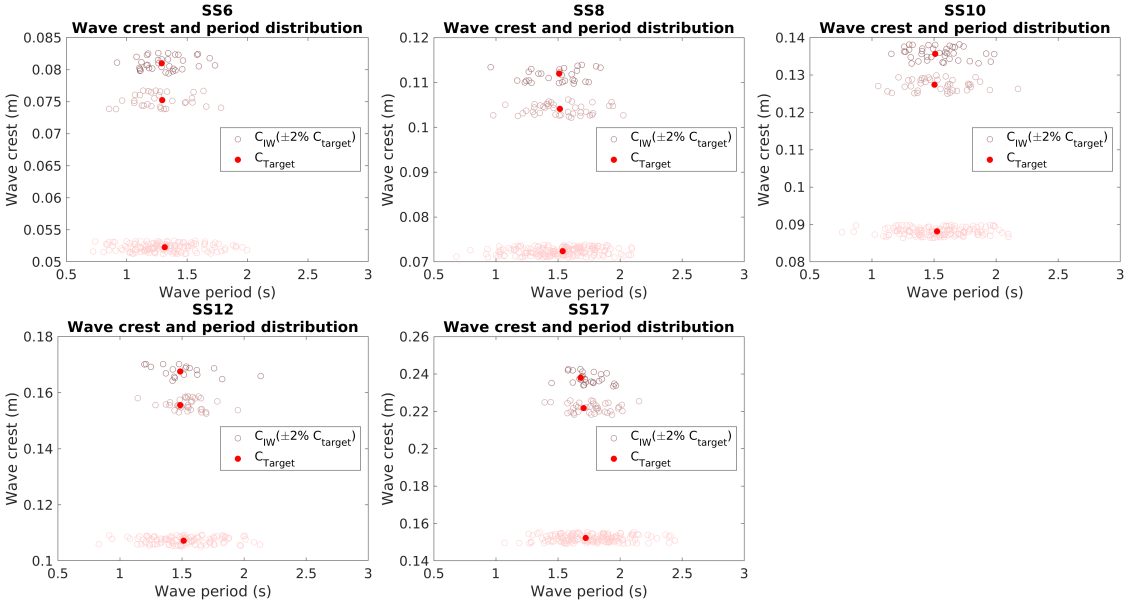

Figure 35: Wave crest and period distribution (model scale)

HOS-NWT successfully implemented the key features of the physical wave tank, and thus the solver accurately generated target irregular wave conditions containing strong nonlinear wave-wave interactions and complex energy dissipation by breaking waves. In the case of the experimental results applying the same wave data, despite a slight difference due to the physical limitations of the experimental settings, it has been confirmed that the shape of the wave spectrum and POE distribution curve are qualitatively and quantitatively comparable to the numerical calculation results. Additionally, from a short-term statistical point of view, it was found that 8 to 12 realizations of a 3-hour wave spectrum for each sea state provided fairly similar wave crest POE distributions up to $Crest/Hs = 1$ corresponding to the POE of around 4×10^{-3}. The Forristall distribution was always steeper than the numerically (or experimentally) estimated ensemble POE curve due to the absence of higher-order above second-order wave effects.

In the case of FORM-based EDW, its elevation and corresponding wave components were calculated by coupling HOS-NWT to the FORM method. The algorithm used for the FORM optimization was the Hasofer and Lind (HL) based algorithm called MHLGA, which applies the merit function to increase its robustness and requires no gradient evaluation of the limit state function to increase the computational efficiency. The numerical and experimental validation of the practicality of the EDW calculation process applying HOS-NWT was performed. All numerically calculated EDWs were generated in the experiment and compared with the measurements. Also, in both the numerical simulation and the experiment, EDW signals were compared with irregular waves that occurred in a given sea state in terms of the overall shape of wave elevation.

A review of the geometrical similarity with the irregular wave signals extracted from several realizations for each sea state confirmed that the FORM-based algorithm provides an EDW profile that is very similar to the average (or most probable) shape of the extracted waves in most cases. Even though some discrepancies in neighboring waves were found for the low POE level cases in severe sea conditions, the overall shape is still comparable. Accordingly, the crest and period distribution of all extracted irregular waves and EDW show that EDW is located almost in the middle of the irregular wave group. The POE value of the target crest C_{target} estimated by the analytical FORM expression agrees very well with the wave brute force result in moderate sea states. However, for EDW cases with low POE levels in severe sea states, the estimated POE by the FORM method is overestimated. The ratio of C_{target}/λ_p is found to be related to the POE estimation result by the FORM method. However, further studies seem to be needed to accurately figure out influencing parameters for the conservative POE estimation by FORM.

To summarize, by applying HOS-NWT to the FORM method, and considering

higher-order wave contributions, the nonlinear focusing wave was calculated for all EDW cases, and we confirm that the calculated EDW is very comparable to the average of nonlinear irregular waves in terms of shape. It can therefore be said that the FORM-based EDW calculation procedure applying HOS-NWT produces a wave scenario that is highly likely to occur in an actual sea state. From a structural response point of view, of course, taking higher-order contributions into consideration in the EDW calculation will also play an important role in predicting accurate structural responses for such abnormal waves.

7. Acknowledgment

The work presented in this paper was supported by Centrale Nantes - Bureau Veritas research chair.

References

Adegeest, L., Braathen, A., Løseth, R., 1998. Use of non-linear sea-loads simulations in design of ships, in: Practical Design of Ships and Other Floating Structures, pp. 53–58.

Bennett, S., Hudson, D., Temarel, P., 2012. A comparison of abnormal wave generation techniques for experimental modelling of abnormal wave–vessel interactions. Ocean engineering 51, 34–48.

Bonnefoy, F., Ducrozet, G., Le Touzé, D., Ferrant, P., 2010. Time domain simulation of nonlinear water waves using spectral methods, in: Advances in Numerical Simulation of Nonlinear Water Waves. World Scientific, pp. 129–164.

Canard, M., Ducrozet, G., Bouscasse, B., 2022. Varying ocean wave statistics emerging from a single energy spectrum in an experimental wave tank. Ocean Engineering 246, 110375.

Chaplin, J.R., 1996. On frequency-focusing unidirectional waves. International Journal of Offshore and Polar Engineering 6.

Clauss, G.n.F., Schmittner, C.E., 2005. Experimental optimization of extreme wave sequences for the deterministic analysis of wave/structure interaction, in: International Conference on Offshore Mechanics and Arctic Engineering, pp. 467–473.

Der Kiureghian, A., 2000. The geometry of random vibrations and solutions by form and sorm. Probabilistic Engineering Mechanics 15, 81–90.

Dietz, J.S., 2005. Application of conditional waves as critical wave episodes for extreme loads on marine structures. Technical University of Denmark.

Dommermuth, D.G., Yue, D.K., 1987. A high-order spectral method for the study of nonlinear gravity waves. Journal of Fluid Mechanics 184, 267–288.

Ducrozet, G., Bonnefoy, F., Le Touzé, D., Ferrant, P., 2006. Implementation and validation of nonlinear wavemaker models in a hos numerical wave tank. International Journal of Offshore and Polar Engineering 16.

Ducrozet, G., Bonnefoy, F., Le Touzé, D., Ferrant, P., 2012. A modified high-order spectral method for wavemaker modeling in a numerical wave tank. European Journal of Mechanics-B/Fluids 34, 19–34.

Ducrozet, G., Fink, M., Chabchoub, A., 2016. Time-reversal of nonlinear waves: Applicability and limitations. Physical Review Fluids 1, 054302.

Fedele, F., Lugni, C., Chawla, A., 2017. The sinking of the el faro: Predicting real world rogue waves during hurricane joaquin. Scientific reports 7, 1–15.

Ghadirian, A., Bredmose, H., Schløer, S., 2017. Prediction of the shape of inline wave force and free surface elevation using first order reliability method (form). Energy Procedia 137, 162–176.

Hansen, P.F., Nielsen, L.P., 1995. On the new wave model for the kinematics of large ocean waves. Technical Report. American Society of Mechanical Engineers, New York, NY (United States).

Hasofer, A.M., Lind, N.C., 1974. Exact and invariant second-moment code format. Journal of the Engineering Mechanics division 100, 111–121.

Huang, Z., Zhang, Y., 2018. Semi-empirical single realization and ensemble crest distributions of long-crest nonlinear waves, in: International Conference on Offshore Mechanics and Arctic Engineering, American Society of Mechanical Engineers. p. V001T01A032.

Hunt-Raby, A.C., Borthwick, A.G., Stansby, P.K., Taylor, P.H., 2011. Experimental measurement of focused wave group and solitary wave overtopping. Journal of Hydraulic Research 49, 450–464.

Jensen, J.J., 2009. Stochastic procedures for extreme wave load predictions–wave bending moment in ships. Marine Structures 22, 194–208.

Jensen, J.J., Capul, J., 2006. Extreme response predictions for jack-up units in second order stochastic waves by form. Probabilistic Engineering Mechanics 21, 330–337.

Jensen, J.J., Choi, J.h., Nielsen, U.D., 2017. Statistical prediction of parametric roll using form. Ocean Engineering 144, 235–242.

Klein, M., Clauss, G.F., Hoffmann, N., 2021. Introducing envelope soliton solutions for wave–structure investigations. Ocean Engineering 234, 109271.

Korean Register, 2017. Guidance on strength assessment of container ships considering the whipping effect. Busan. Korea .

Lemaire, M., 2013. Structural reliability. John Wiley & Sons.

Lindgren, G., 1970. Some properties of a normal process near a local maximum. The Annals of Mathematical Statistics 41, 1870–1883.

Lindgren, G., 1984. Use and structure of slepian model processes for prediction and detection in crossing and extreme value theory, in: Statistical extremes and applications. Springer, pp. 261–284.

Liu, P.L., Der Kiureghian, A., 1991. Optimization algorithms for structural reliability. Structural safety 9, 161–177.

Nocedal, J., Wright, S., 2006. Numerical optimization. Springer Science & Business Media.

Santos, S., Matioli, L., Beck, A., 2012. New optimization algorithms for structural reliability analysis. Computer Modeling in Engineering & Sciences(CMES) 83, 23–55.

Schmittner, C., Hennig, J., 2012. Optimization of short-crested deterministic wave sequences via a phase-amplitude iteration scheme, in: International Conference

on Offshore Mechanics and Arctic Engineering, American Society of Mechanical Engineers. pp. 79–86.

Schmittner, C., Kosleck, S., Hennig, J., 2009. A phase-amplitude iteration scheme for the optimization of deterministic wave sequences, in: International Conference on Offshore Mechanics and Arctic Engineering, pp. 653–660.

Seiffert, B.R., Ducrozet, G., 2018. Simulation of breaking waves using the high-order spectral method with laboratory experiments: wave-breaking energy dissipation. Ocean Dynamics 68, 65–89.

Seiffert, B.R., Ducrozet, G., Bonnefoy, F., 2017. Simulation of breaking waves using the high-order spectral method with laboratory experiments: Wave-breaking onset. Ocean Modelling 119, 94–104.

Suret, P., Tikan, A., Bonnefoy, F., Copie, F., Ducrozet, G., Gelash, A., Prabhudesai, G., Michel, G., Cazaubiel, A., Falcon, E., et al., 2020. Nonlinear spectral synthesis of soliton gas in deep-water surface gravity waves. Physical Review Letters 125, 264101.

Tian, Z., Perlin, M., Choi, W., 2010. Energy dissipation in two-dimensional unsteady plunging breakers and an eddy viscosity model. Journal of fluid mechanics 655, 217–257.

Torhaug, R., 1996. Extreme response analysis of non-linear ocean structures: identification of minimal stochastic wave input for time domain simulation. Ph.D. thesis. PhD Dissertation, Department of Civil Engineering, Standford University ....

Tromans, P.S., Anaturk, A.R., Hagemeijer, P., 1991. A new model for the kinemat-

ics of large ocean waves-application as a design wave, in: The first international offshore and polar engineering conference, OnePetro.

Walker, D.A., Taylor, P.H., Taylor, R.E., 2004. The shape of large surface waves on the open sea and the draupner new year wave. Applied Ocean Research 26, 73–83.

Walker, D.A., Taylor, R.E., 2005. Wave diffraction from linear arrays of cylinders. Ocean Engineering 32, 2053–2078.

West, B.J., Brueckner, K.A., Janda, R.S., Milder, D.M., Milton, R.L., 1987. A new numerical method for surface hydrodynamics. Journal of Geophysical Research: Oceans 92, 11803–11824.

Zang, J., Taylor, P.H., Morgan, G., Stringer, R., Orszaghova, J., Grice, J., Tello, M., 2010. Steep wave and breaking wave impact on offshore wind turbine foundations–ringing re-visited, in: 25th International Workshop on Water Waves and Floating Bodies, pp. 9–12.